physica status solidi pss

www.interscience.wiley.com

reprints

WILEY-VCH

REPRINT

Phys. Status Solidi B **247**, No. 4, 829–845 (2010) / **DOI** 10.1002/pssb.200945434

physica status solidi b
www.pss-b.com
basic solid state physics

Feature Article

Modeling quantum dot lasers with optical feedback: sensitivity of bifurcation scenarios

Christian Otto*, **Kathy Lüdge, and Eckehard Schöll**

Institut für Theoretische Physik, Technische Universität Berlin, Hardenbergstraße 36, 10623 Berlin, Germany

Received 16 September 2009, revised 3 December 2009, accepted 14 December 2009
Published online 29 January 2010

PACS 42.55.Px, 42.60.Da, 85.35.Be

* Corresponding author: e-mail otto@itp.physik.tu-berlin.de, Phone: +49 30 31424474, Fax: +49 30 31421130

We present a systematic study of the complex dynamics of a quantum dot (QD) laser subjected to optical feedback from a short external cavity. Our model consists of a Lang–Kobayashi like model for the electric field combined with a microscopically based rate equation system. We separately treat electron and hole dynamics in the QDs and the surrounding wetting layer (WL). By tuning the phase–amplitude coupling and the optical confinement factor we are able to discuss various scenarios of the dynamics on the route towards conventional quantum well (QW) lasers. Due to the optical feedback, multistability occurs in our model in form of external cavity modes (ECMs) or delay-induced intensity pulsations. In dependence of the feedback strength we analyze complex bifurcation scenarios for the intensity of the emitted laser light as well as time series, power spectra, and phase portraits of all dynamic variables in order to elucidate the internal dynamics of the laser.

1 Introduction Quantum dot (QD) injection lasers are an important optoelectronic application of self-organized semiconductor QD structures [1]. Based on their density of states they exhibit unique properties like low threshold current, large temperature stability, and low feedback sensitivity [2]. A microscopic theory of QD light emitters is reviewed in Ref. [3]. Experimental results with QD lasers subjected to optical feedback showed that due to the smaller α-factor and the strongly suppressed relaxation oscillations (ROs) QD lasers show stable operation for a wider range of optical feedback strength [4–6] and the route to chaos can be observed more clearly [7]. While optical feedback can lead to instabilities in laser applications it can also significantly improve the modulation bandwidth of directly modulated lasers [8]. Moreover the self-pulsations of a semiconductor laser subjected to optical feedback can be useful for signal processing applications [9]. A comprehensive overview of the topic is given in Ref. [10]. A review from the nonlinear dynamics point of view focusing on the laser instabilities is given in Ref. [11] and for optical injection in Ref. [12]. Such systems with optical feedback also provide examples for the stabilization of steady states (cw emission) or periodic oscillations (self-pulsations) by time delayed feedback control [13–17] or bubbling in coupled lasers [18].

In this work we will systematically model the complex dynamics of a QD laser with optical feedback using a microscopically based rate equation system for the carrier dynamics as described in Ref. [19] and the Lang–Kobayashi model for the electric field in the cavity [20]. In the literature a lot of attention has been paid to the bifurcation scenarios of conventional quantum well (QW) lasers with optical feedback [21–25], however, besides the work of [26] regarding the long-cavity regime, systematic studies of the dynamics of QD laser in the short-cavity regime are still missing. Our simulations focus on this regime as introduced by Schunk and Petermann [27]. The authors define an external cavity as short if the product of the RO frequency and the external cavity round-trip time is considerably less than unity. Our focus to the short cavity regime is motivated as follows. On the one hand the short cavities are of great interest for technologic applications, where multi-section devices with short integrated cavities are dominant. On the other hand the short cavity regime is interesting from a dynamical system point of view, because of its medium complexity. In the short cavity regime the stability of the laser output depends on the phase of the light that is coupled back into the cavity [28]. Instead of low frequency fluctuations (LFFs) [22, 29] and coherence collapse (CC) found in QW devices with

feedback, the QD laser system displays regular intensity pulsation in a certain range of the feedback strength which we show to be strictly regular for small linewidth enhancement factor α. For increasing α more irregular pulses are found that resemble those found in Ref. [30] for QW lasers with a short external cavity length.

The paper is organized as follows: after introducing our model approach in Section 2 and the external cavity modes (ECMs) in Section 3, we will study the bifurcation scenarios of the laser output that occur by changing the feedback strength K in Section 4. In Section 5 the impact of the linewidth enhancement factor α and the optical confinement factor Γ on the first laser instability will be discussed. In Section 6 we compare the stability properties of the QD laser to those of a QW laser described by a conventional three-variable Lang–Kobayashi model, before we conclude in Section 7.

2 Quantum dot laser model with feedback In order to model the dynamics of the QD laser with optical feedback we consider a two-section device, consisting of a gain section of length L that contains the layers of self-organized QDs as active medium, and a feedback section given by a mirror at a distance l to the end facet of the QD laser, reflecting light back into the gain region. The schematic setup is shown in Fig. 1. The gain section of the QD laser is modeled by a microscopically based rate equation system as described in Refs. [19, 31]. It allows for separate treatment of electron and hole dynamics in the QDs as well as in the surrounding wetting layer (WL) and has been shown to yield quantitative agreement with turn-on experiments of QD lasers [32]. The energy scheme of the QD laser is shown in Fig. 2.

However, the introduction of an optical feedback requires a model that takes into account also the phase of the electrical field and not only the photon density, thus the field equation has to be complex. We use a Lang–Kobayashi like equation for the slowly varying amplitude of the electrical field [20], because it has been shown that despite several limitations it describes even complex phenomena for QW lasers remarkably well [25], including bifurcation scenarios of stable cw emission, periodic behavior, regular, and irregular pulse packages. A derivation and the necessary approximations of the Lang–Kobayashi model can be found

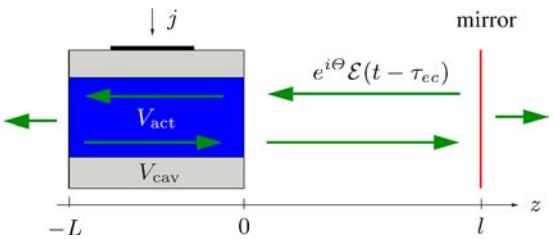

Figure 1 (online color at: www.pss-b.com) Schematic setup of the considered QD laser device with optical feedback from a short external cavity.

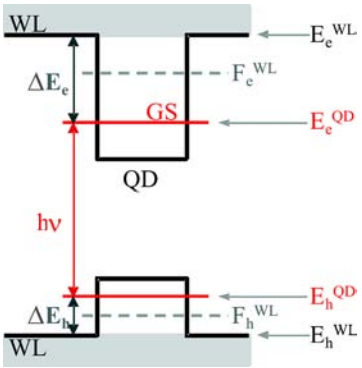

Figure 2 (online color at: www.pss-b.com) Energy diagram of the QD and WL system.

in Ref. [33]. Combined with the QD laser gain model from Ref. [19] the field equation is given by:

$$\dot{\mathcal{E}} = (1 - i\alpha)\frac{1}{2}\{\Gamma WA(n_e + n_h - N^{QD}) - 2\kappa\} + \frac{K}{\tau_{in}} e^{i\Theta}\mathcal{E}_{\tau_{ec}} + F_{\mathcal{E}}(t). \quad (1)$$

Here $\mathcal{E} = \sqrt{N_{ph}(t)}\, e^{-i\phi(t)}$ is the normalized slowly varying complex amplitude of the electrical field given in polar coordinates by the photon number N_{ph} and the phase ϕ. The linear gain $\Gamma WA(n_e + n_h - N^{QD})$ contains the optical confinement factor Γ, the Einstein coefficient W, the area of the active region A, and the inversion $n_e + n_h - N^{QD}$, given by the two-dimensional electron and hole density in the QDs n_e and n_h, respectively. N^{QD} denotes twice the density of the active QDs, taking into account spin degeneracy. The optical intensity loss is given by 2κ, and α is the linewidth enhancement factor. K is the strength of the optical feedback. The phase shift of the light during one round trip in the external cavity ($\tau_{ec} = 2l/c$) is given by $\Theta = \omega_{th}\tau_{ec}$ with ω_{th} denoting the frequency of the solitary laser at the lasing threshold. For the modeling Θ is treated as an independent variable. This is justified because for the considered optical wavelength of $\lambda = 1.3\,\mu m$ a small variation of the cavity length l has large impact on the phase Θ without considerably changing τ_{ec}. The field labeled by the subscript τ_{ec}, $\mathcal{E}_{\tau_{ec}}$, and therewith $n_{ph,\tau_{ec}}$ and $\phi_{\tau_{ec}}$, are the electric field amplitude, the photon density, and the optical phase taken at the delayed time $t - \tau_{ec}$. The time τ_{in} is given by the single-pass time of the gain region $\tau_{in} = L/c_m$ where c_m is the speed of light inside the gain region.

The spontaneous emission in the field Eq. (1) is taken into account by a complex Gaussian white noise term $F_{\mathcal{E}}(t) = F'_{\mathcal{E}}(t) + iF''_{\mathcal{E}}(t)$, where $F'_{\mathcal{E}}(t)$ is the real part of the complex stochastic variable and $F''_{\mathcal{E}}(t)$ is its imaginary part. Evaluated at any time t these are real normal distributed random variables with zero mean that are uncorrelated:

$$\langle F_{\mathcal{E}}(t)F^*_{\mathcal{E}}(t')\rangle = \beta AR_{sp}\delta(t - t')$$

$$\left\langle F_a(t)F_b^*(t')\right\rangle = \frac{1}{2}\beta A R_{\rm sp}\delta_{\rm ab}\delta(t-t').$$

In the above equations the asterisk * denotes the complex conjugate, β is the spontaneous emission factor, $R_{\rm sp}$ is the spontaneous emission rate, and $F_{a,b}$ are chosen as real- or imaginary parts of $F_{\mathcal{E}}$. Thus the field equation is a complex stochastic differential equation (SDE) (Langevin equation). The goal is to transform the complex SDE for $\mathcal{E}$ (Eq. 1) into two real SDEs for the photon density $n_{\rm ph} = N_{\rm ph}/A$ and the phase ϕ. Neglecting the stochastic term this is just a transformation to polar coordinates. Including the additive noise term Ito's formula [34] can be used. In Ref. [14] a precise description is given how to apply Ito's formula in this case. Averaging over the stochastic terms after the Ito transformation the final rate equations for the photon density $n_{\rm ph}$, the phase of the electric field ϕ, and the four equations for the densities of electrons and holes in the QDs ($n_{\rm e}$ and $n_{\rm h}$) and in the WL ($w_{\rm e}$ and $w_{\rm h}$) read:

$$\dot{n}_{\rm ph} = -2\kappa n_{\rm ph} + \Gamma R_{\rm ind}(n_{\rm e},n_{\rm h},n_{\rm ph}) + \beta R_{\rm sp}(n_{\rm e},n_{\rm h}) + 2\frac{K}{\tau_{\rm in}}\sqrt{n_{{\rm ph},\tau_{\rm ec}}n_{\rm ph}}\,\cos(\phi-\phi_{\tau_{\rm ec}}+\Theta) \tag{2a}$$

$$\dot{\phi} = \frac{\alpha}{2}\{\Gamma WA(n_{\rm e}+n_{\rm h}-N^{\rm QD})-2\kappa\} - \frac{K}{\tau_{\rm in}}\sqrt{\frac{n_{{\rm ph},\tau_{\rm ec}}}{n_{\rm ph}}}\,\sin(\phi-\phi_{\tau_{\rm ec}}+\Theta) \tag{2b}$$

$$\dot{n}_{\rm e} = -\frac{n_{\rm e}}{\tau_{\rm e}(w_{\rm e},w_{\rm h})} + S_{\rm e}^{\rm in}(w_{\rm e},w_{\rm h})N^{\rm QD} - R_{\rm ind}(n_{\rm e},n_{\rm h},n_{\rm ph}) - R_{\rm sp}(n_{\rm e},n_{\rm h}) \tag{2c}$$

$$\dot{n}_{\rm h} = -\frac{n_{\rm h}}{\tau_{\rm h}(w_{\rm e},w_{\rm h})} + S_{\rm h}^{\rm in}(w_{\rm e},w_{\rm h})N^{\rm QD} - R_{\rm ind}(n_{\rm e},n_{\rm h},n_{\rm ph}) - R_{\rm sp}(n_{\rm e},n_{\rm h}) \tag{2d}$$

$$\dot{w}_{\rm e} = \frac{j(t)}{e_0} + \frac{n_{\rm e}}{\tau_{\rm e}(w_{\rm e},w_{\rm h})}\frac{N^{\rm sum}}{N^{\rm QD}} - S_{\rm e}^{\rm in}(w_{\rm e},w_{\rm h})N^{\rm sum} - \tilde{R}_{\rm sp}(w_{\rm e},w_{\rm h}) \tag{2e}$$

$$\dot{w}_{\rm h} = \frac{j(t)}{e_0} + \frac{n_{\rm h}}{\tau_{\rm h}(w_{\rm e},w_{\rm h})}\frac{N^{\rm sum}}{N^{\rm QD}} - S_{\rm h}^{\rm in}(w_{\rm e},w_{\rm h})N^{\rm sum} - \tilde{R}_{\rm sp}(w_{\rm e},w_{\rm h}) \tag{2f}$$

According to Ref. [19] the induced processes of absorption and emission are modeled by a linear gain $R_{\rm ind}(n_{\rm e},n_{\rm h},n_{\rm ph}) = WA(n_{\rm e}+n_{\rm h}-N^{\rm QD})n_{\rm ph}$. The spontaneous emission rate in the QDs is approximated by bimolecular recombination $R_{\rm sp}(n_{\rm e},n_{\rm h}) = (W/N^{\rm QD})n_{\rm e}n_{\rm h}$. The spontaneous emission rate in the WL is given by $\tilde{R}_{\rm sp}(w_{\rm e},w_{\rm h}) = B^{\rm S}w_{\rm e}w_{\rm h}$ where $B^{\rm S}$ is the band–band recombination coefficient in the WL. $\Gamma = \Gamma_{\rm g}N^{\rm QD}/N^{\rm sum}$ is the optical confinement factor. It is the product of the geometric confinement factor $\Gamma_{\rm g}$ (i.e., the ratio of the volume of all QDs and the optical mode volume) and the ratio $N^{\rm QD}/N^{\rm sum}$, where the density $N^{\rm sum}$ is twice the total QD density as given by experimental surface imaging (accounting for reduced gain because due to the size distribution of the QDs only a subgroup of all QDs, namely the active QDs $N^{\rm QD}$, match the mode energy for lasing). j is the injection current density and e_0 is the elementary charge. The values of all the parameters used in our simulations are listed in Table 1.

Another crucial contribution to the dynamics in the gain region is given by the non-radiative carrier–carrier scattering rates $S_{\rm e}^{\rm in}$ and $S_{\rm h}^{\rm in}$ for electron and hole capture from the WL into the QD levels, $S_{\rm e}^{\rm out}$ and $S_{\rm h}^{\rm out}$ for carrier escape from the QD levels, and scattering times $\tau_{\rm e} = (S_{\rm e}^{\rm in}+S_{\rm e}^{\rm out})^{-1}$ and $\tau_{\rm h} = (S_{\rm h}^{\rm in}+S_{\rm h}^{\rm out})^{-1}$. Microscopically, the electron in- and out-scattering rates can be calculated as:

$$S_{\rm e}^{\rm in} = \sum_{klmb'} W_{klmb'}^{\rm in} f_k f_l (1-f_m) \qquad (k\to{\rm QD},\ l\to m)$$

$$S_{\rm e}^{\rm out} = \sum_{klmb'} W_{klmb'}^{\rm out} (1-f_k)(1-f_l) f_m \quad ({\rm QD}\to k,\ m\to l)$$

where the transition probabilities $W_{klmb'}^{\rm in/out}$ contain the screened Coulomb matrix elements and the energy-conserving δ-function [31], and f_k, f_l, and f_m are the occupation probabilities of the respective WL states, and analogously for holes. Note that those rates depend nonlinearly on the WL carrier densities $w_{\rm e}$ and $w_{\rm h}$. Assuming quasi-equilibrium within the four ensembles of carriers, i.e., electrons and holes in the QDs and electrons and holes in the WL, but non-equilibrium between these ensembles, the in- and out-scattering rates can be related within the framework of detailed balance (see Ref. [19] for a thorough discussion):

$$S_{\rm e}^{\rm in} = S_{\rm e}^{\rm out}\exp\left\{\frac{F_{\rm e}^{\rm WL}-E_{\rm e}^{\rm QD}}{kT}\right\}, \tag{3}$$

Table 1 Numerical parameters used in the simulation unless stated otherwise (same parameters as in Ref. [19]).

symbol	value	symbol	value
W	$0.7\,{\rm ns}^{-1}$	A	$4\times10^{-5}\,{\rm cm}^2$
α	0.9	$N^{\rm QD}$	$0.6\times10^{10}\,{\rm cm}^{-2}$
2κ	$0.1\,{\rm ps}^{-1}$	$N^{\rm sum}$	$20\times10^{10}\,{\rm cm}^{-2}$
$\Gamma_{\rm g}$	0.075	β	5×10^{-6}
Γ	2.25×10^{-3}	$B^{\rm S}$	$540\,{\rm ns}^{-1}\,{\rm nm}^2$
Θ	π	$\tau_{\rm in}(L)$	24 ps (1 nm)
T	300 K	$\tau_{\rm ec}(l)$	160 ps (25 nm)
$\Delta E_{\rm e}$	101 meV	$\Delta E_{\rm h}$	54 meV
$m_{\rm e}$	$0.043\ m_0$	$m_{\rm h}$	$0.45\ m_0$
λ	1.3 μm	$\omega_{\rm th}/2\pi$	230 THz

$$S_{\mathrm{h}}^{\mathrm{in}} = S_{\mathrm{h}}^{\mathrm{out}} \exp\left\{\frac{E_{\mathrm{h}}^{\mathrm{QD}} - F_{\mathrm{h}}^{\mathrm{WL}}}{kT}\right\}. \tag{4}$$

In the above equations $E_{\mathrm{e}}^{\mathrm{QD}}$ and $E_{\mathrm{h}}^{\mathrm{QD}}$ are the confined QD electron and hole energy levels, respectively. The quasi-Fermi levels F_b^{WL} (see Fig. 2) for electrons ($b = \mathrm{e}$) and holes ($b = \mathrm{h}$) in the WL depend on the carrier densities in the WL w_{b}. They are given by:

$$F_{\mathrm{e}}^{\mathrm{WL}}(w_{\mathrm{e}}) = E_{\mathrm{e}}^{\mathrm{WL}} + kT \ln\left[\exp\left(\frac{w_{\mathrm{e}}}{\rho_{\mathrm{e}} kT}\right) - 1\right], \tag{5}$$

$$F_{\mathrm{h}}^{\mathrm{WL}}(w_{\mathrm{h}}) = E_{\mathrm{h}}^{\mathrm{WL}} - kT \ln\left[\exp\left(\frac{w_{\mathrm{h}}}{\rho_{\mathrm{h}} kT}\right) - 1\right]. \tag{6}$$

Here, E_b^{WL} denote the WL band-edges, $\rho_b = m_b/(\pi\hbar^2)$ are the 2D effective densities of states in the WL with the parameters m_{b} used for the effective masses (in units of the electron mass m_0), T is temperature and k is the Boltzmann constant. Introducing the energy differences $\Delta E_{\mathrm{e}} = E_{\mathrm{e}}^{\mathrm{WL}} - E_{\mathrm{e}}^{\mathrm{QD}}$ and $\Delta E_{\mathrm{h}} = E_{\mathrm{h}}^{\mathrm{QD}} - E_{\mathrm{h}}^{\mathrm{WL}}$ (see Table 1), the relation between the in- and out-scattering rates can be expressed as:

$$S_b^{\mathrm{in}}(w_{\mathrm{e}}, w_{\mathrm{h}}) = S_b^{\mathrm{out}}(w_{\mathrm{e}}, w_{\mathrm{h}})\, \mathrm{e}^{\Delta E_b/kT}\left[\mathrm{e}^{w_b/\rho_b kT} - 1\right]. \tag{7}$$

The corresponding analytic fitting functions for the microscopically calculated scattering rates [19] are given in Appendix A.

3 External cavity modes Basic solutions of Eq. (2a–f) are special rotating wave solutions of the electric field. They are called ECMs and will be explained in the following. The total optical field E is normalized to the square root of the number of photons in the cavity $|E|^2 = N_{\mathrm{ph}}$. As mentioned above the field is taken in the slowly varying envelope approximation:

$$E(t) = \mathcal{E}(t)\, \mathrm{e}^{-\mathrm{i}\omega_{\mathrm{th}} t}, \tag{8}$$

i.e., assuming the field to be a product of the slowly varying amplitude $\mathcal{E}$ and a fast oscillating carrier wave $\mathrm{e}^{-\mathrm{i}\omega_{\mathrm{th}} t}$ that oscillates with the frequency of the solitary laser at the laser threshold ω_{th}. It is important to note that the phase $\phi(t)$ of the complex field amplitude is also time dependent. Thus, the actual frequency of the laser deviates in general from ω_{th} due to the influence of the optical feedback.

For the analysis of the fixed points of the system we first note, that the dynamical system consisting of the Eqs. (1) and (2c)–(2d) is invariant under the continuous symmetry group of all rotations in the complex plane $S^1 \equiv \{c \in \mathbb{C} \text{ with } |c| = 1\}$. That means that the rotation over any angle $\theta = \arg(c)$ of the trajectory is again a trajectory. Thus a solution of the dynamical equations is either S^1 invariant itself, or it is not isolated but comes as a rotational family parametrized by the elements of S^1. Such a family of solutions:

$$S^1 \circ (\mathcal{E}, n_{\mathrm{e}}, n_{\mathrm{h}}, w_{\mathrm{e}}, w_{\mathrm{h}})_{t_0}^{t_1} = \{(c\mathcal{E}, n_{\mathrm{e}}, n_{\mathrm{h}}, w_{\mathrm{e}}, w_{\mathrm{h}})_{t_0}^{t_1} | c \in S^1\}, \tag{9}$$

is called a group orbit. It consists of all images of the trajectory starting at t_0 and ending up at t_1 under all rotations of S^1 [35].

The S^1 symmetry is a consequence of two properties: one is the linearity of the field Eq. (1) with respect to $\mathcal{E}$, and the other is the fact that only the modulus $|\mathcal{E}|$ of the electrical field amplitude enters into the carrier Eqs. (2e) and (2f) through the photon density $n_{\mathrm{ph}} = |\mathcal{E}|^2/A$ [10]. The simplest solutions that are S^1 invariant are the ECMs, which are continuous wave (cw) solutions with constant photon number $N_{\mathrm{ph,s}}$ and carrier densities $n_{\mathrm{e,s}}$, $n_{\mathrm{h,s}}$, $w_{\mathrm{e,s}}$, $w_{\mathrm{h,s}}$, and a phase ϕ that varies linearly with time:

$$\begin{aligned}&(\mathcal{E}(t), n_{\mathrm{e}}(t), n_{\mathrm{h}}(t), w_{\mathrm{e}}(t), w_{\mathrm{h}}(t))\\ &\quad = (\sqrt{N_{\mathrm{ph,s}}}\, \mathrm{e}^{-\mathrm{i}\Delta\omega_{\mathrm{s}} t}, n_{\mathrm{e,s}}, n_{\mathrm{h,s}}, w_{\mathrm{e,s}}, w_{\mathrm{h,s}}).\end{aligned} \tag{10}$$

An ECM oscillates with the deviation from the solitary laser threshold frequency $\Delta\omega_{\mathrm{s}} = \omega - \omega_{\mathrm{th}}$. Each ECM is a group orbit of the S^1-symmetry, which means that in a projection on a hyperplane spanned by the photon density n_{ph} and the carrier densities it is just one point. That is why ECMs are often referred to as steady state solutions in the literature. A complete discussion of the symmetries for conventional and phase conjugated optical feedback is given in Ref. [36].

Neglecting spontaneous emission βR_{sp} below the laser threshold, a "trivial" solution with $\mathcal{E} \equiv 0$ is stable. At the laser threshold this solution changes stability and ECM solutions have to be considered [17]. Inserting the ECM ansatz Eq. (10) into the dynamical equations (2a)–(2f) yields:

$$\begin{aligned}0 = &\{\Gamma W A(n_{\mathrm{e,s}} + n_{\mathrm{h,s}} - N^{\mathrm{QD}}) - 2\kappa\} n_{\mathrm{ph,s}}\\ &+ 2\frac{K}{\tau_{\mathrm{in}}} n_{\mathrm{ph,s}} \cos(\Delta\omega_{\mathrm{s}}\tau_{\mathrm{ec}} + \Theta),\end{aligned} \tag{11a}$$

$$\begin{aligned}\Delta\omega_{\mathrm{s}} = &\frac{\alpha}{2}\{\Gamma W A(n_{\mathrm{e,s}} + n_{\mathrm{h,s}} - N^{\mathrm{QD}}) - 2\kappa\}\\ &- \frac{K}{\tau_{\mathrm{in}}} \sin(\Delta\omega_{\mathrm{s}}\tau_{\mathrm{ec}} + \Theta),\end{aligned} \tag{11b}$$

$$\dot{n}_{\mathrm{e}} = \dot{n}_{\mathrm{h}} = \dot{w}_{\mathrm{e}} = \dot{w}_{\mathrm{h}} = 0. \tag{11c}$$

Here we have introduced the steady state photon density $n_{\mathrm{ph,s}}$. Using the condition $n_{\mathrm{ph,s}} \neq 0$ that is valid above threshold and inserting Eq. (11a) into Eq. (11b) yields the following form of the transcendental equation for the frequency deviations $\Delta\omega_{\mathrm{s}}$:

$$\Delta\omega_{\mathrm{s}} = -\frac{K}{\tau_{\mathrm{in}}}\{\alpha \cos(\Delta\omega_{\mathrm{s}}\tau_{\mathrm{ec}} + \Theta) - \sin(\Delta\omega_{\mathrm{s}}\tau_{\mathrm{ec}} + \Theta)\}. \tag{12}$$

This can be rewritten as:

$$\Delta\omega_s = -\frac{K_{\rm eff}}{\tau_{\rm ec}}\sin(\Delta\omega_s\tau_{\rm ec} + \Theta + \arctan(\alpha)), \qquad (13)$$

where we have introduced an effective feedback strength:

$$K_{\rm eff} = K\frac{\tau_{\rm ec}}{\tau_{\rm in}}\sqrt{1+\alpha^2}. \qquad (14)$$

Solving the transcendental Eq. (13) yields the ECM frequencies as a function of the feedback strength K, the internal cavity single-pass time $\tau_{\rm in}$, the α-factor and the phase with which the light is coupled back into the cavity Θ. For $K_{\rm eff} < 1$ Eq. (13) has only one solution. This is the ECM, which develops out of the solitary laser mode at $K = 0$. For gradually increasing K new ECMs are created pairwise in saddle-node bifurcations. (The first pair is created at $K_{\rm eff} = 1$.) In the literature the node solutions are often referred to as modes and the saddle solutions as antimodes. Figure 3ii and iv shows the ECM frequencies $\Delta\omega_s$ of the modes (blue solid) and antimodes (blue dotted) as a function of K for $\alpha = 0.9$ and 3.2, respectively. One branch of solutions (antimodes) is always unstable due to destructive interference between laser field and delayed field (inner branches closest to $\Delta\omega_s = 0$ dashed in Fig. 3ii and iv), and the other branch (modes) is stable but may eventually experience a change of stability through a Hopf bifurcation [21, 37, 38].

4 Bifurcation scenarios This section will discuss the dynamics of the QD laser as a function of feedback strength K and the linewidth enhancement factor α. As mentioned above modeling the short cavity regime results in sensitivity of the laser output to the phase Θ of the electric field. The feedback phase is fixed to $\Theta = \pi$ and is only treated as a tunable parameter in Section 4.1.3 below. Numerically obtained bifurcation diagrams as well as time series, power spectra, and phase portraits will be discussed in order to elucidate the internal dynamics of the laser.

4.1 Bifurcation cascade for $\alpha = 0.9$ (small) In the following simulations the gain section of the QD laser with feedback is pumped at a current of $j = 2.5 j_{\rm th}$ ($j_{\rm th}$ is the threshold current density without feedback) starting at time $t = 0$. To illustrate the influence of the optical feedback Fig. 4 shows the response of the photon density $n_{\rm ph}$ to a rectangular current density $j(t)$ without feedback $K = 0$ (blue dashed line) and with feedback $K = 0.98$ (red dash-dotted line). The current starts at $t = 0$ and has a width of 10 ns. After a delay time of 0.8 ns where the laser builds up the inversion the laser performs ROs. Without feedback ($K = 0$) they are strongly damped as it is typical for QD lasers [19]. With increasing K the ROs become weakly damped as shown for $K = 0.98$.

4.1.1 Intensity pulsations For gradually increasing feedback strength K the local minima and maxima of the laser output, i.e., of the photon density, are recorded between $t = 300$ and 350 ns and plotted in a bifurcation diagram as shown in Fig. 3i. Note that the long integration time is chosen in order to avoid transient effects of the turn-on dynamics in the laser output. For small $K < K_c = 0.099$ the laser shows stable cw operation at the first ECM. At $K_c = 0.099$ the ECM loses stability in a supercritical Hopf bifurcation leading to a small stable limit cycle, i.e., to a solution with periodically modulated photon density (self-sustained intensity pulsation). Thus, the bifurcation diagram for $K > K_c$ (see Fig. 3i and the blowup Fig. 3v) shows two branches: the maxima and minima of the limit cycle oscillations. The two branches scale like the square root of the distance from the bifurcation point. This is the signature of a Hopf bifurcation. For $K = 0.11$ time series and power spectrum of these periodic pulsations are shown in Fig. 5a (corresponding to the vertical blue dash-dotted line (a) in Fig. 3v). The frequency of $\nu_{\rm RO}(K = 0.11) = 2.46$ GHz is the RO frequency as expected for higher pump currents [37] and can be recognized by the most prominent peak in the power spectrum in Fig. 5a. Higher frequency peaks are higher harmonics. (Note that Ref. [37] also discussed the Lang–Kobayashi equations in the limit of very small pump currents close to the threshold and showed that the frequency of the instability is determined by the external cavity roundtrip time.) Projections of the trajectory onto the ($n_{\rm e/h}$, $n_{\rm ph}$)-planes as well as onto the ($w_{\rm e/h}$,$n_{\rm ph}$)-planes show motions on a stable limit cycle. This can be seen in the first row of Fig. 6 where the four different phase space projections are displayed. The value of the cw laser operation directly before the Hopf bifurcation is indicated by black dots in the phase space projections. Due to the fact that in our model electrons and holes have separate degrees of freedom described by different microscopic scattering rates $S_{\rm e/h}^{\rm in/out}$, the shape of the projected limit cycles is different for electrons and holes.

With further increase of the feedback strength K the system undergoes a period doubling route to chaos with windows of period two and three at $K = 0.17$ and 0.203 that are indicated as vertical blue dash-dotted lines (b) and (c) in the bifurcation diagram (Fig. 3v). The corresponding time series and power spectra are depicted in Fig. 5b and c, respectively. In the power spectra the peaks at $\nu_{\frac{1}{2}{\rm RO}}(0.17) = 1.42$ GHz and $\nu_{\frac{1}{2}{\rm RO}}(0.203) = 1.03$ GHz and $\nu_{\frac{2}{3}{\rm RO}}(0.203) = 2.09$ GHz on the lower frequency sides of the dominant peaks of the ROs ($\nu_{\rm RO}(0.17) = 2.84$ GHz and $\nu_{\rm RO}(0.203) = 3.14$ GHz) can be observed clearly. They correspond to twofolded and threefolded limit cycles in the phase space projection shown in Fig. 6b and c. At $K = 0.21$ (d) the laser output is chaotic (dense dots at fixed K in the bifurcation diagram Fig. 3i and 3v), which can also be seen in the broad power spectrum of Fig. 5d and the large chaotic attractor in the phase space projections (Fig. 6d). The time series displays irregular pulse packages, that are modulated with the frequency of the ROs. Two distinct frequencies are still observable in the power spectrum: the main peak can be attributed to the ROs at $\nu_{\rm RO}(0.21) = 3.22$ GHz and the lower

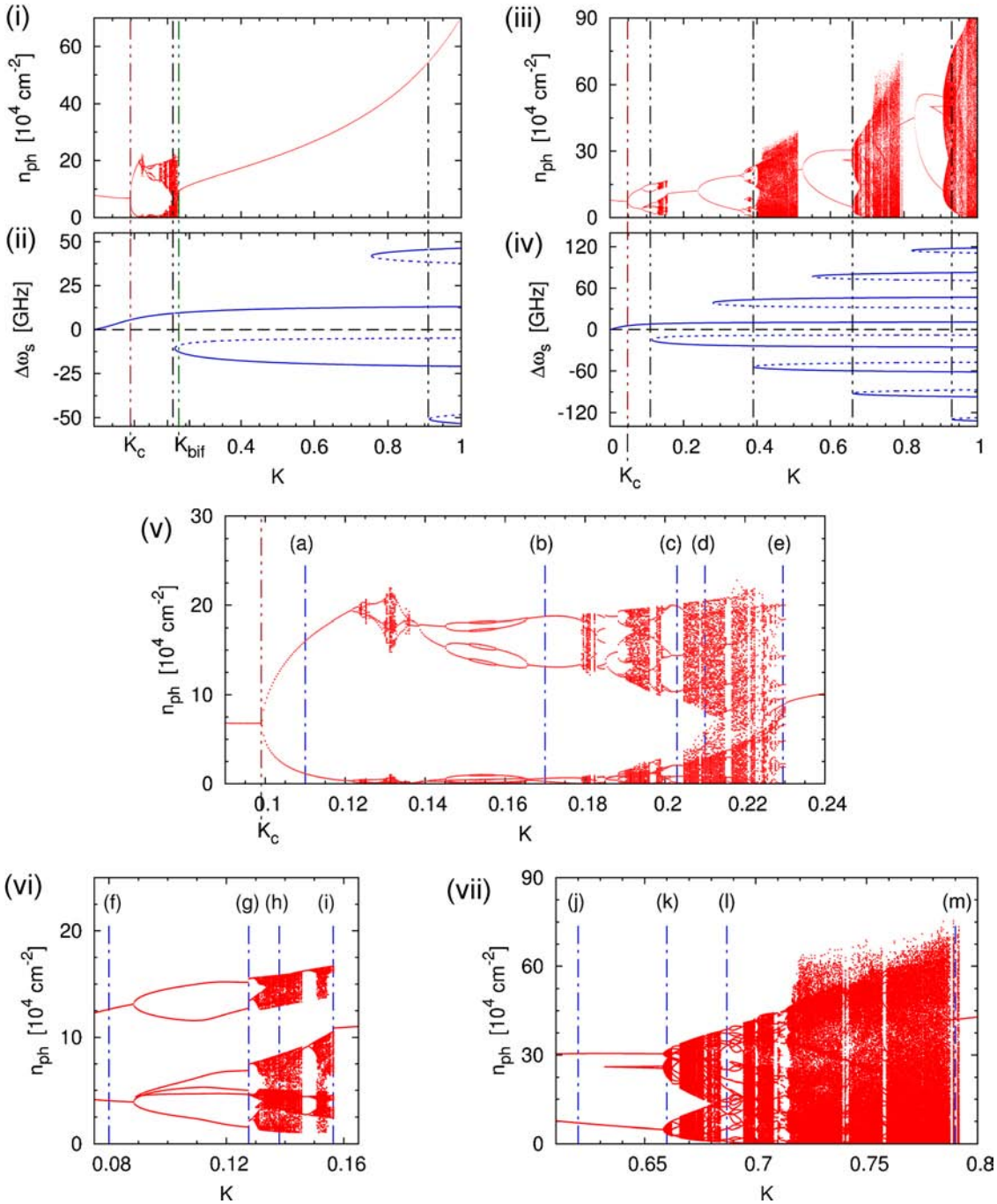

Figure 3 (online color at: www.pss-b.com) Bifurcation diagrams of the photon density n_{ph} (red) and frequency deviations $\Delta\omega_s$ of the possible external cavity modes (blue) in dependence of the feedback strength K for small $\alpha = 0.9$ (i and ii) and large $\alpha = 3.2$ (iii and iv). Blue solid and dotted lines denote ECM modes and anti-modes, respectively. Panel (v) shows a blowup of the bifurcation cascade for small $\alpha = 0.9$ and (vi and vii) show blowups of the first and the third bifurcation cascade for large $\alpha = 3.2$.

frequency peak at $\nu_{PP}(0.21) = 0.69$ GHz belongs to the envelope of the pulse packages.

4.1.2 Regular pulse packages So far the discussion was limited to the regime of feedback strengths K where only one ECM, i.e., the one that can be continued out of the solitary laser solution, is available to the QD laser. This is proven by Fig. 3ii that depicts the solutions for the frequency deviation $\Delta\omega_s$ determined from Eq. (13). At $K = 0.215$ a new pair of ECMs (mode and antimode) is born in a saddle-node bifurcation. In all cases the electrons and holes clearly display desynchronized dynamics. Thus, a new stable fixed point (node) as well as a saddle-point are available to the system dynamics. As a consequence we observe another

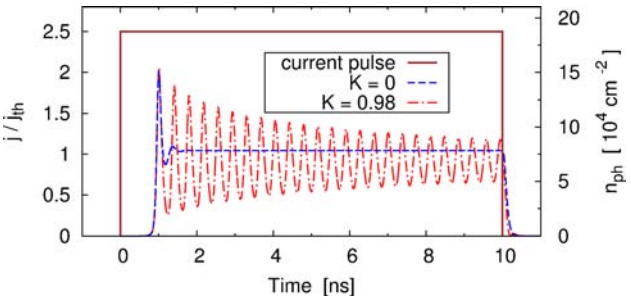

Figure 4 (online color at: www.pss-b.com) Response of photon density n_{ph} to a rectangular current density $j(t)$ of 10 ns width (brown line) for a feedback strength of $K = 0.98$ (red dash-dotted line) and without feedback $K = 0$ (blue dashed line). $j(t)$ is normalized to the threshold current density without feedback j_{th}. Other parameters as in Table 1.

drastic change of the laser dynamics towards stable cw operation: at the bifurcation point $K_{bif} = 0.2305$ a global bifurcation takes place. Due to the typical scaling discussed later, we presume it to be a homoclinic bifurcation of a limit cycle. This can be seen in the bifurcation diagram in Fig. 3i and the blowup Fig. 3v that show only one single branch beyond K_{bif}. In a small range of K values before these global bifurcation we observe bistability: trajectories starting close to the saddle-point of the first ECM are attracted by a delay-induced limit cycle, whereas trajectories starting elsewhere (not shown here) end up in a stable node.

In the output of the laser this delay induced limit cycle is manifested by regular pulse packages as they are depicted in Fig. 5e. Looking at the phase space projections of Fig. 6e it can be seen that starting from a maximum intensity point of one pulse package the excursion through the (n_e, n_{ph})-space is similar to the turn-on dynamics of the QD-laser as the trajectory spirals towards a certain point in phase space [19]. However, in this case it is a saddle-focus (the first ECM has already lost its stability), which is the reason why the trajectory does not reach the fixed point but is repelled to a low intensity region along the unstable manifold of the saddle. What follows is a re-injection ending at the same maximum photon intensity, which completes the cycle. As the second ECM solution already exists, trajectories starting close to this will not enter the limit cycle but directly approach the stable fixed point of the second ECM (bistability). The steady state photon- and carrier-densities of the first ECM laser solution at K_c (directly before it becomes unstable) are indicated by black dots in Fig. 6. Open brown circles denote the steady state densities of the second ECM mode at $K = 0.2295$. The high frequency modulation of the pulse packages is still the RO frequency $\nu_{RO}(0.2295) = 3.66\,\mathrm{GHz}$, however, the lower frequency given by the interpulse interval depends strongly on the feedback strength K and thus on the distance to the global bifurcation. In Fig. 7 the distance in time between two pulse packages T (interpulse interval time) is plotted as a function of $\ln|K - K_{bif}|$ (see also Fig. 6e). The points lie on a straight line, thus T scales like $T \propto a \ln|(K - K_{bif})|$ with $a = -1.23$,

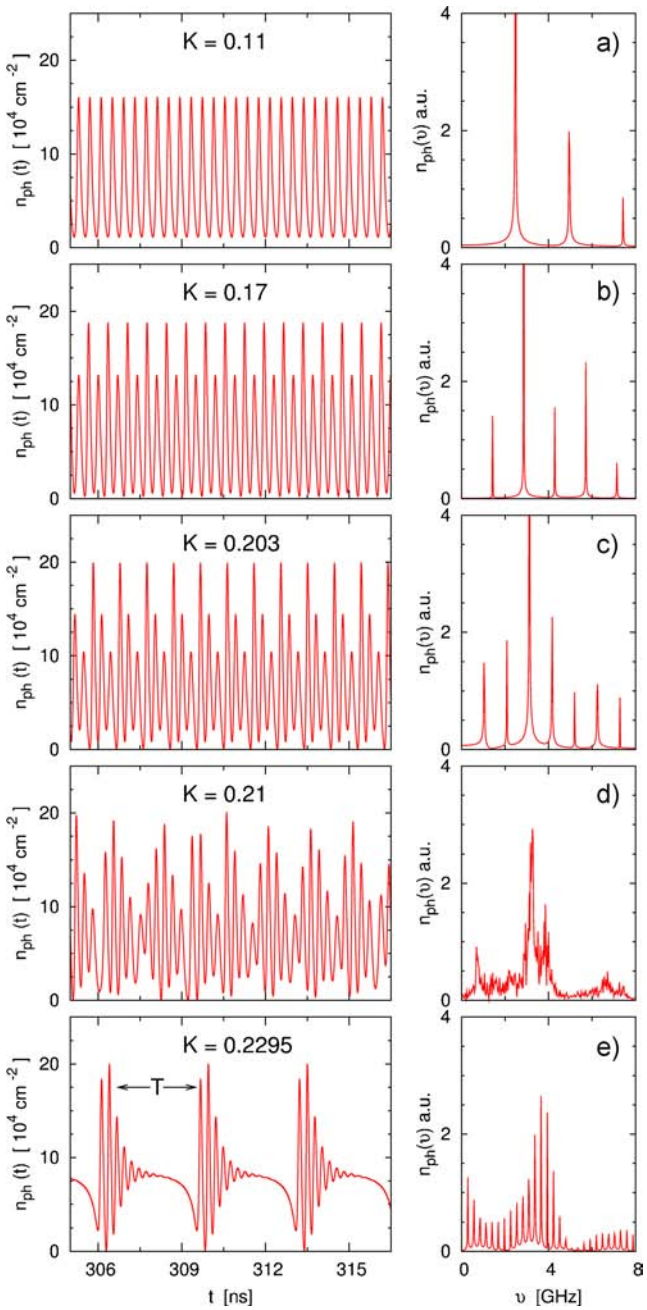

Figure 5 (online color at: www.pss-b.com) Time series (left) and power spectra (right) for selected feedback strengths K: rows (a–e) correspond to $K = 0.11 - 0.2295$ as indicated by vertical blue dash-dotted lines (a–e) in the bifurcation cascade for small $\alpha = 0.9$ and $\Gamma = 0.00225$ in Fig. 3v. T denotes the interpulse interval time.

underlining the logarithmic scaling of the period of the limit cycle with the distance to the bifurcation point K_{bif}. This behavior is typical for a homoclinic bifurcation of limit cycles. Near this bifurcation the system scales like $T \approx -\lambda_\mu^{-1} \ln|K - K_{bif}|$, where λ_μ is the real part of the least unstable eigenvalue of the saddle-focus [39]. It is important to note that the center of the spiral motion of the trajectory in

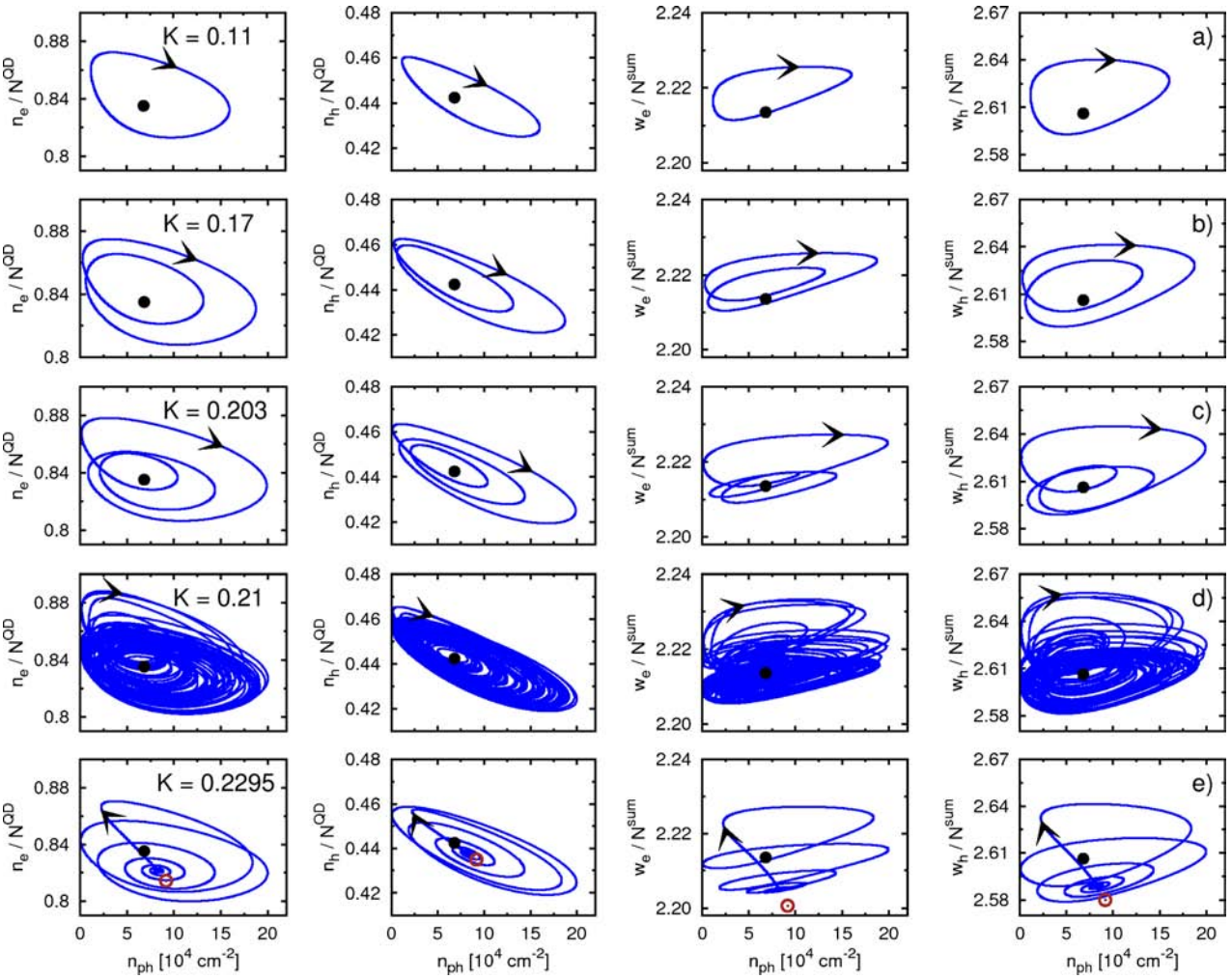

Figure 6 (online color at: www.pss-b.com) Phase space projections of the trajectory onto planes spanned by the photon density n_{ph} and the carrier densities n_e, n_h, w_e, and w_h (column 1–4). Rows (a–e) correspond to $K = 0.11 - 0.2295$ as indicated by vertical blue dash-dotted lines (a–e) in the bifurcation cascade for small $\alpha = 0.9$ and $\Gamma = 0.00225$ in Fig. 3v. Black dots indicate the steady state of the first ECM before the supercritical Hopf bifurcation at $K_c = 0.099$. Brown circles indicate the second stable ECM at $K = 0.2295$.

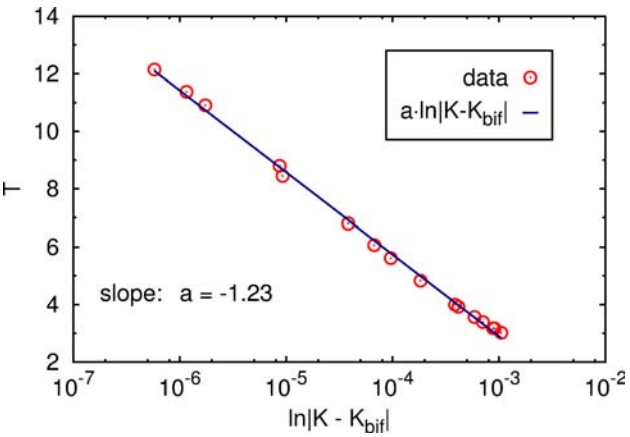

Figure 7 (online color at: www.pss-b.com) Scaling of the interpulse interval time T near the homoclinic bifurcation ($K_{bif} = 0.2305$) for small $\alpha = 0.9$ and $\Gamma = 0.00225$.

Fig. 6e, representing the regular intensity pulsations, does not match with the steady state densities of the second ECM (open brown circles). The reason is that for the chosen initial conditions the system can only access this new attractor after the homoclinic bifurcation [40]. Comparing the projections of the attractor of the chaotic trajectories at $K = 0.21$ (vertical dash-dotted line (d) in Fig. 3v) shown in the four phase space projections in Fig. 6d with the limit cycle projections in Fig. 6e striking similarities can be found. The only difference is that during one period the trajectory of the regular pulses closes up while in the case of the periodic attractor it is smeared out. Thus what we see at $K = 0.21$ is Shilnikov chaos associated with the saddle-focus which later on undergoes the homoclinic bifurcation at which the stable and the unstable manifolds merge.

Note that the pulse packages found by Heil et al. [30] for QW lasers with short external cavity are not identical to those just described. The two main difference are: at first their modulation frequency is the external round trip time which

can be attributed to the much lower pump current as discussed in Ref. [37]. Second, the pulses are only close to regular and do not form closed limit cycles. Simulations show that in our QD model the homoclinic bifurcation forming the strictly regular pulses cannot be found for α-factor higher than 0.9 meaning that this parameter plays a crucial role. For $\alpha = 3.2$, as will be discussed in Section 4.2, we find pulse packages similar to the ones reported in Ref. [30].

4.1.3 Phase dependence As Heil et al. [25] have shown for QW lasers with short external cavity, the sensitivity of the laser to optical feedback depends strongly on the phase Θ of the electric field after the round trip through the external cavity. So far the phase was set to $\Theta = \pi$, however, in this section we will discuss changes of the laser output that are related to changes in Θ.

To avoid confusions with existing literature note that a lot of studies about the Lang–Kobayashi system ([24, 33, 38, 41] use the phase $\Phi = \Theta + \arctan(\alpha)$ for their analytic discussions. This is motivated by the transcendental Eq. (13) because it yields symmetric results for $\Phi = 0$ and $\Phi = \pi$. For the chosen $\alpha = 0.9$ this corresponds to $\Theta = 1.77\pi$ and 0.77π, respectively.

We start our discussion of the phase dependence with the phase $\Theta = 0.77\pi$. As depicted in Fig. 8ii the ECM solution for the electric field is first described by $\Delta\omega_s = 0$ before two more solutions are born in a pitchfork bifurcation at $K_c = 0.11$. In contrast to the case $\Theta = \pi$ that was discussed earlier, the bifurcation diagram shows stable cw operation of the laser for all feedback strengths (see the continuous line in Fig. 8i). Only a kink at K_c is observed which accounts for the fact that the laser operation changes to the maximum gain mode at the bitchfork bifurcation point.

If the phase is further decreased to $\Theta = 0$ as was done in Fig. 8iii and iv (corresponding to constructive interference between $\mathcal{E}$ and $\mathcal{E}_{\tau_{ec}}$) we observe stable laser operation until $K_c = 0.537$. Behind this point we find one bifurcation cascade that is shown in the bifurcation diagram of Fig. 8iii. If compared to the previously discussed case of $\Theta = \pi$ (shown in Fig. 3ii) several changes have to be marked. To begin with, the first ECM is stable over a large range of feedback strength K and loses stability via a subcritical Hopf bifurcation at K_c. The system directly jumps to a stable limit cycle (like in Ref. [42]) and does not show the square root like increase of the limit cycle amplitude. This indicates a subcritical Hopf bifurcation, which can be explained by the mode structure of the ECMs. Contrary to the case of $\Theta = \pi$, where the first ECM pair appears at positive frequency shifts $\Delta\omega_s$, the first saddle-node bifurcation appears for positive $\Delta\omega_s$ (referring to a low gain mode). Only later on at $K = 0.57$ the ECM pair with higher gain is born as depicted in Fig. 8iv. At $K = 0.547$ the system undergoes a quasiperiodic route to chaos. The time series shows oscillations at the RO frequency modulated slightly (like in the case of $K = 0.66$) but less regularly, with irregular power dropouts. At $K = 0.567$ an interior crisis takes place. The attractor collides with a saddle and the system settles

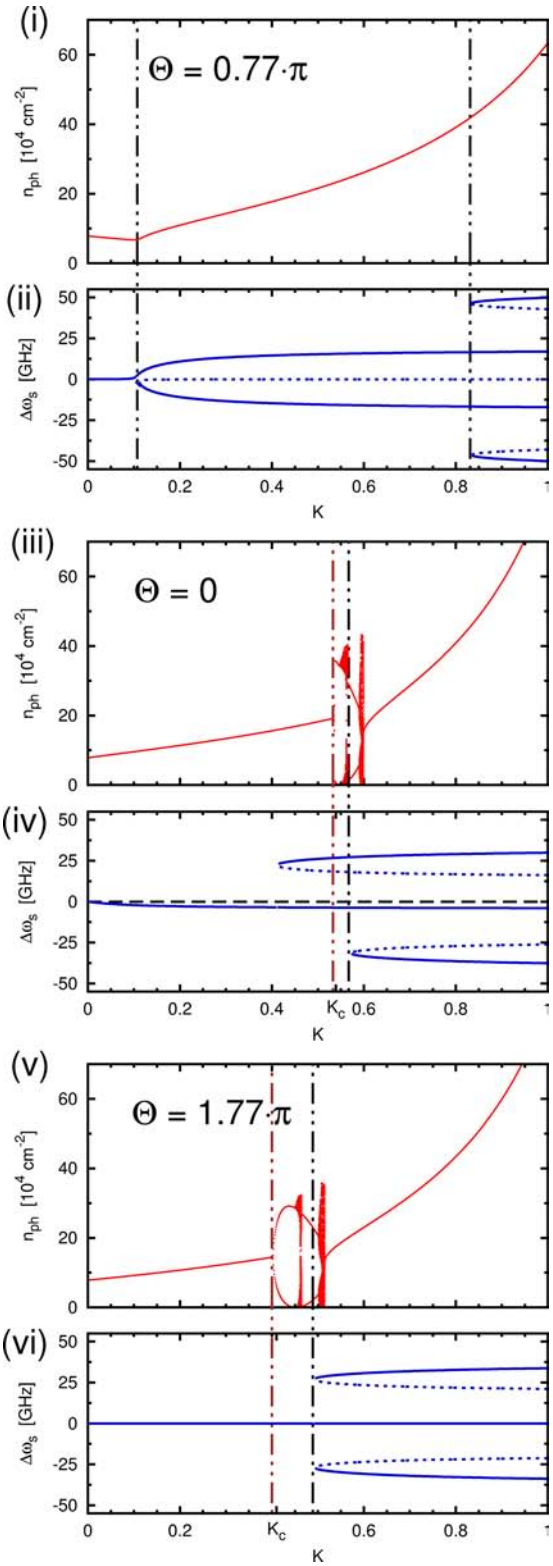

Figure 8 (online color at: www.pss-b.com) Bifurcation diagrams of the photon density (i, iii, and v) and frequency deviations of the possible ECMs (ii, iv, and vi) as a function of the feedback strength K for three different values of the feedback phase Θ. (i and ii): $\Theta = 0.77\pi$, (iii and iv): $\Theta = 0$, and (v and vi): $\Theta = 1.77\pi$. Parameters: $\alpha = 0.9$ and $\Gamma = 0.00225$.

down to a period-one limit cycle. At $K = 0.5932$ a supercritical Hopf (Neimark–Sacker) bifurcation introduces another incommensurate frequency. In the phase space projections the trajectories now roll up densely on the surface of a torus and in the bifurcation diagram of Fig. 8iii we observe a broadening of the maxima and minima of the oscillations. The time series shows ROs modulated by the lower newly introduced incommensurate frequency. With increasing K the modulation become more pronounced forming fairly regular pulse packages. In the phase space projections the torus gains in volume. However the power spectra suggest that the system does not become chaotic but stays quasiperiodic. At $K = 0.5986$ a homoclinic bifurcation of limit cycles takes places, similar to the one for $\Theta = \pi$ shown in Fig. 3v, point (e). We find again the typical logarithmic scaling of the interpulse interval time with the distance of the bifurcation point. For larger K the laser settles down to the ECM (the stable node solution of the ECM-pair) and performs cw operation up to the maximum physically relevant feedback strength of $K = 1.0$.

If we further decrease the phase to $\Theta = 1.77\pi \equiv -0.23\pi$ the ECMs again show the $\Delta\omega_s = 0$ solution over a wide range of feedback strength. At $K = 0.49$ two simultaneous saddle-node bifurcations take place and lead to the emergence of two saddle and two node solutions (see Fig. 8vi). The corresponding bifurcation diagram of Fig. 8v shows the same main features as discussed for $\Theta = 0$, only the first instability at a lower feedback strength of $K_c = 0.4$ is a supercritical Hopf bifurcation. It is followed by a quasiperiodic route to chaos at $K = 0.45$, an interior crisis, and a torus bifurcation at $K = 0.5$. At $K = 0.515$ the unstable operation ends with a homoclinic bifurcation with the typical logarithmic scaling of the interpulse interval.

If we proceed the path of decreasing phase, the critical feedback strength K_c further decreases and the bifurcations observed in the cascade become more complex (see the case $\Theta = \pi \equiv -\pi$ discussed in the previous sections and shown in Fig. 3ii). Further decreasing the phase Θ closes the 2π interval and arrives at the already discussed symmetric case $\Theta = 0.77\pi \equiv -2.77\pi$. Here the critical feedback strength is minimal, however at this point it is not a Hopf bifurcation point as the laser stays stable. Beyond this value of the phase the critical feedback strength K_c is again very high and describes a subcritical Hopf bifurcation.

To sum up, experiments measuring the sensitivity of a QD laser to optical feedback in the short cavity regime have to be aware of the phase Θ in order to give comparable results. Our results show that for $\alpha = 0.9$ the value $\Theta = 0.77\pi$ allows to stabilize the laser over the whole range of feedback strength.

4.2 Bifurcation cascades for $\alpha = 3.2$ (large) The most important features of QD lasers if compared to QW lasers are the internal carrier dynamics resulting in strongly damped RO oscillations and the much smaller coupling between phase and amplitude of the light field. Therefore the last section presented the results for ''typical'' QD lasers with small $\alpha = 0.9$. For a more systematic understanding and comparison to QW lasers this section will elucidate the influence of the linewidth enhancement factor α and discuss the bifurcation scenarios for $\alpha = 3.2$.

Figure 3iii presents the bifurcation diagram of the photon density for $\alpha = 3.2$ as a function of the feedback strength. The frequency deviations of the ECMs $\Delta\omega_s$ in Fig. 3iv are calculated numerically from Eq. (12). At first glance two striking differences can be seen compared to the ''typical'' QD laser case in Fig. 3i and ii: first, the sensitivity to the feedback is increased (the stable regions are much shorter) which results in a series of bifurcation cascades, and second, the number of ECM solutions that are available to the laser is augmented by a factor of 2. The larger number of ECMs is the reason for the larger number of bifurcation cascades, because with increasing K each initially stable ECM eventually loses stability via a Hopf bifurcation [24] followed by a route to chaos. The first two cascades perform a period-doubling route to chaos while the third and the fourth cascade take a quasiperiodic route to chaos. Similar bifurcation diagrams have also been found numerically and experimentally for QW lasers in the short cavity regime [23, 25]. However, besides the larger α-factor our laser model still contains the material equations of the QD laser. This allows us to focus on the internal dynamics of the laser and clarify its impact.

In the first bifurcation cascade the laser performs a period-doubling route to chaos starting at $K_c = 0.048$ with a supercritical Hopf bifurcation (brown vertical dash-dotted line in Fig. 3iii and iv. An enlargement of the first bifurcation cascade is shown in Fig. 3vi. The blue vertical dash-dotted lines (f–i) indicate the value of the feedback strength K, at which time series, power spectra, and phase space projections are evaluated. For $K = 0.08$ Fig. 9f depicts the regular pulsation of the photon output at a frequency of $\nu_{RO}(0.08) = 2.71\,\mathrm{GHz}$, which are the undamped ROs after the first supercritical Hopf bifurcation. All phase space projections in Fig. 10f show period-one limit cycles with small amplitude. The shape of the limit cycles is slightly deformed by the reminiscence of the attractor of the first ECM for $K < K_c$. Such ''attractor-ruins'' have already been suggested by Mørk et al. [21]. The steady state densities of this ECM directly before K_c are indicated by black dots in Fig. 10. As it can be seen in Fig. 3iv a new pair of ECMs is created at $K = 0.117$. Behind this point the system shows multistability. At $K = 0.088$ the second period doubling bifurcation takes place. Figure 10g shows a period-2 limit circle at $K = 0.1276$ (vertical line (g) in Fig. 3vi). The small loop in the projection onto the (n_{ph}, n_h)-plane is again caused by the ghost of the attractor for $K < K_c$. This loop corresponds to the small maxima in the time series in Fig. 9g. The power spectrum shows the peak of the RO's at $\nu_{RO}(0.1276) = 2.36\,\mathrm{GHz}$ and a lower frequency peak at $\nu_{\frac{1}{2}RO}(0.1276) = 1.20\,\mathrm{GHz}$, which indicates that a period-doubling bifurcation has taken place. The other peaks are higher harmonics and sums and differences of these basic frequencies. While the dynamics of electrons and holes in the

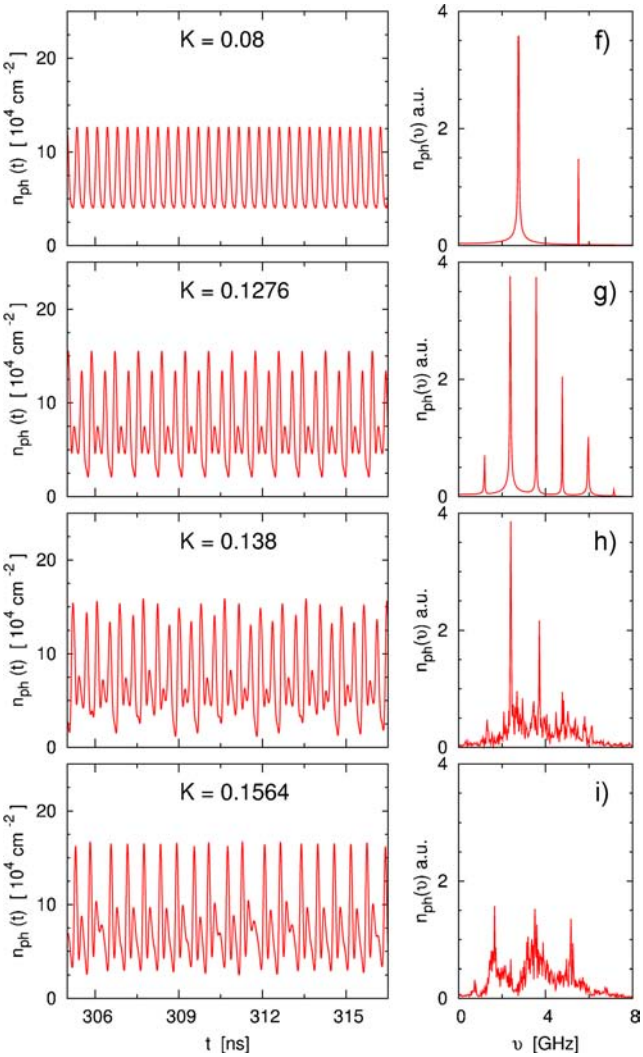

Figure 9 (online color at: www.pss-b.com) Time series (left) and power spectra (right) for selected feedback strengths K: rows (f–i) correspond to $K = 0.08 - 0.16$ as indicated by vertical blue dash-dotted lines (f–i) in the first bifurcation cascade for large $\alpha = 3.2$ and $\Gamma = 0.00225$ in Fig. 3vi.

QDs is still decoupled, the phase space projections of the trajectory onto the (n_{ph}, w_e)- and (n_{ph}, w_h) planes show much less differences.

With increasing feedback strength the system becomes chaotic by period-doubling. For example at a feedback rate of $K = 0.138$ (h) the period-2 limit cycle has evolved into a strange attractor as can be seen in Fig. 10h. This attractor covers a larger phase space volume, but its shape is still similar to the one of the period-2 cycle. The time evolution is chaotic as can be seen in Fig. 9h, however, it still contains the old mode structure. On top of the broad power spectrum the RO peak at $\nu_{RO}(0.138) = 2.36\,\mathrm{GHz}$ and the peak at half the RO frequency $\nu_{\frac{1}{2}RO}(0.138) = 1.2\,\mathrm{GHz}$ are still visible. Increasing K further we find a periodic window followed by another chaotic region. At $K = 0.1564$ (i), directly before the breakdown of the chaotic attractor, the time series shows fairly regular intensity pulsations that are interrupted by short irregular spiking (see Fig. 9i). This indicates intermittency, with the period-2 pulsations as laminar phase and the spiking as short chaotic outbursts. The phase space projections in Fig. 10i show that the attractor has still the shape of a broadened period-2 orbit. After the bifurcation cascade the system settles down to the second ECM that is stable since its creation at $K = 0.117$. To show that both attractors do not merge the steady state densities of this mode have been indicated by brown circles in the (n_{ph}, $n_{e,h}$)-planes in Fig. 10i. The corresponding WL carrier densities $w_e = 2.19N^{sum}$ and $w_h = 2.56\,N^{sum}$ are outside the plot range and therefore not visible in the (n_{ph}, $w_{e,h}$)-projections of Fig. 10i.

The second ECM becomes unstable in a supercritical Hopf bifurcation at $K = 0.225$. This triggers the start of the second bifurcation cascade. The route to chaos is interrupted by frequency locking in a window from $K = 0.384$ to 0.398 as can be seen in the bifurcation diagram Fig. 3iii. At $K = 0.41$ the bifurcation diagram shows a sudden increase of the attractor volume. According to Sano [22] this is an interior crisis, a global bifurcation where the chaotic attractor of the second ECM merges with the newly born saddle of the third ECM. At the end of the second cascade we observe a boundary crisis. In this global bifurcation the chaotic attractor collides with its basin boundary.

For the third bifurcation cascade we find a quasiperiodic route to chaos which is qualitatively different to the route of the two cascades that have been discussed so far. An enlargement of the bifurcation diagram is shown in Fig. 3vii, again containing the blue dash-dotted lines (j–m) that represent the K values at which the laser dynamics is evaluated. At $K = 0.512$ the fourth ECM changes stability in a supercritical Hopf bifurcation, giving rise to delay-induced intensity pulsations (undamped ROs). These are shown as time series and power spectra in Fig. 11j for $K = 0.62$. The frequency of the RO oscillations is $\nu_{RO}(0.62) = 4.99\,\mathrm{GHz}$ (main peak in the power spectrum). The phase space projections in Fig. 12j show the corresponding limit cycle that is slightly deformed due to the reminiscence of the attractor of the fourth ECM which is stable until the Hopf bifurcation at $K = 0.5122$. This "attractor-ruin" is shown by the black dots in Fig. 12, indicating the steady state densities of the fourth ECM directly before its first Hopf bifurcation. At $K = 0.61$ a new frequency is introduced into the system by a secondary Hopf (Neimark–Sacker) bifurcation. As a consequence the attractor becomes a torus. Contrary to the period-doubling route to chaos this frequency is incommensurate to the RO frequency. Thus trajectories do not close up and hence they are rolling up densely on the surface of the torus. Figure 11k shows the time series and the power spectrum for this motion. The main oscillation with the RO frequency $\nu_{RO}(0.66) = 4.99\,\mathrm{GHz}$ is modulated by a much lower frequency of $\nu_{PP}(0.66) = 1.02\,\mathrm{GHz}$. This frequency is roughly the difference between the external cavity roundtrip frequency $\nu_{ec} = 6.25\,\mathrm{GHz}$ and the RO frequency. With

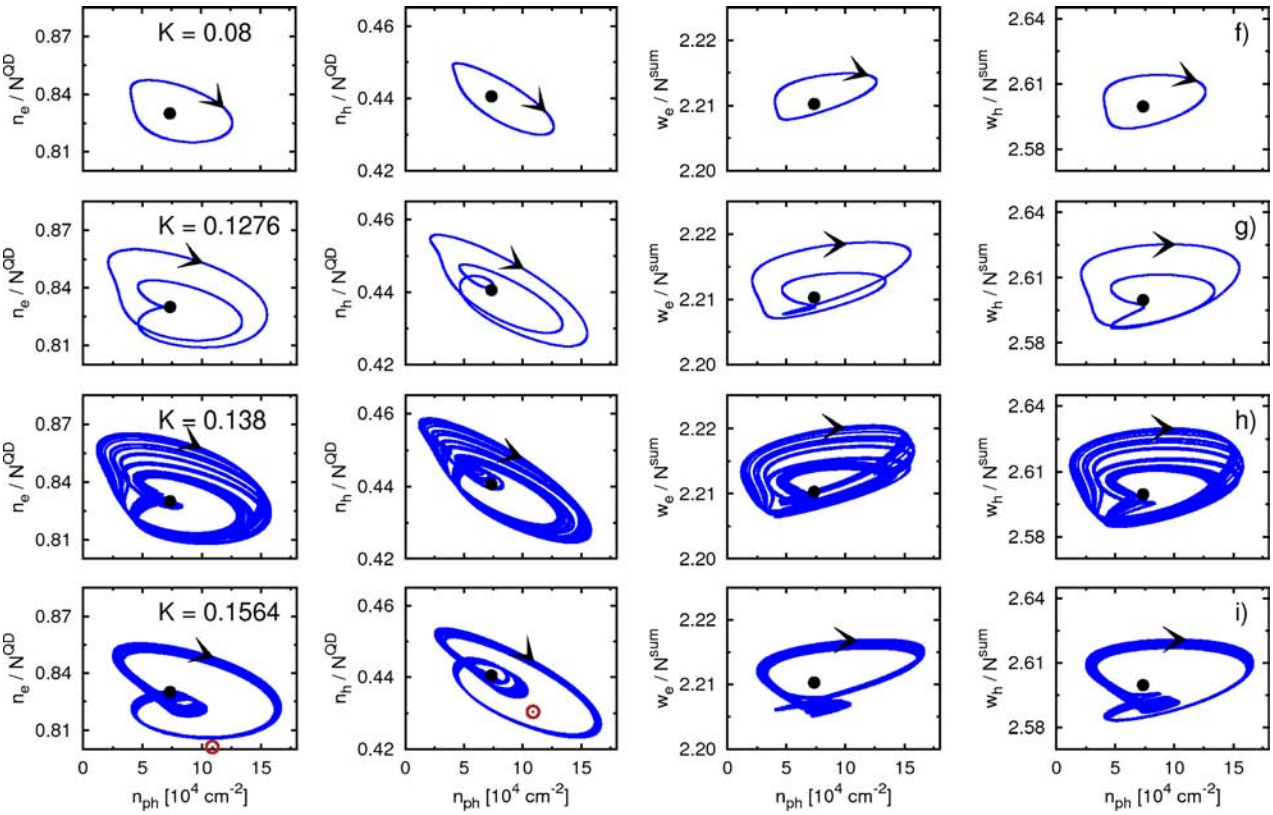

Figure 10 (online color at: www.pss-b.com) Phase space projections of the trajectory onto planes spanned by the photon density n_{ph} and the carrier densities n_e, n_h, w_e, and w_h (column 1–4). Rows (f–i) correspond to $K = 0.08 - 0.1564$ as indicated by vertical blue dash-dotted lines (f–i) in the first bifurcation cascade for large $\alpha = 3.2$ and $\Gamma = 0.00225$ in Fig. 3vi. Black dots indicate the steady state of the first ECM before the supercritical Hopf bifurcation at $K_c = 0.048$. Brown circles indicate the second stable ECM at $K = 0.1564$.

increasing K the modulation will become more and more pronounced forming fairly regular pulse packages towards the end of the bifurcation cascade. The corresponding phase portraits are depicted in Fig. 12k. They show the projections of a torus with similar shape as the limit cycle after the first Hopf bifurcation. The small additional maxima in the time series and the dips in the phase space projections are still due to the attractor-ruin of the fourth ECM.

For increasing K the torus continuously gains height and covers a larger area of the phase space. This process is interrupted by periodic windows, which are created by frequency locking. That means that the two frequencies ν_{RO} and ν_{PP} become commensurate and thus the trajectories lock up on the surface of the torus forming a stable limit cycle. For $K = 0.687$ we find, for example, a cycle of period-6. Its time series in Fig. 11l displays regular pulse packages. The corresponding power spectrum shows the characteristic peaks at $1/6$, $2/6$, ..., of the RO frequency $\nu_{RO}(0.687) = 5.7$ GHz. The phase space projections are shown in Fig. 12l. The shape of the limit cycle is rather complicated due to the complicated mode structure that exists in the cavity at this high feedback rate.

At $K = 0.719$ the torus breaks up into a chaotic attractor. This is accompanied by an abrupt increase in the size of the attractor. Heil et al. [25] who also observed this global bifurcation by varying the feedback phase identified it as an interior crisis, i.e., with a collision of the chaotic attractor of the ECM that became unstable in the cascade with a saddle-point of an other ECM pair. In our case that could be the collision of the fourth ECM with the saddle-point (antimode) of the sixth ECM pair that is created at $K = 0.66$. For $K \geq 0.719$ the saddle is absorbed into the chaotic attractor, resulting in an attractor of much larger size. For $K \geq 0.691$, directly after the periodic window (see Fig. 3vii), the system starts to exhibit bistability between the attractor that developed out of the fourth mode and the stable sixth mode.

The time series and power spectra of the laser output at $K = 0.79$, shortly before the breakdown of the attractor at $K = 0.7905$ are shown in Fig. 11m. We observe pulse packages that are quite regular. They are not completely regular like those found for low $\alpha = 0.9$, because trajectories of adjacent pulse packages do not close up exactly (see Fig. 12m). So each package starts with slightly different initial conditions. In between the pulses the output power drops to 0. Thus, this behavior resembles the LFFs found in QW lasers [23]. The power spectrum still shows the ghost of the old mode structure. The trajectories of these almost regular pulse packages cover a large volume in phase space (see Fig. 12m). Note the larger scale of the ordinate of Fig. 12m in comparison to the other plots of this figure. The

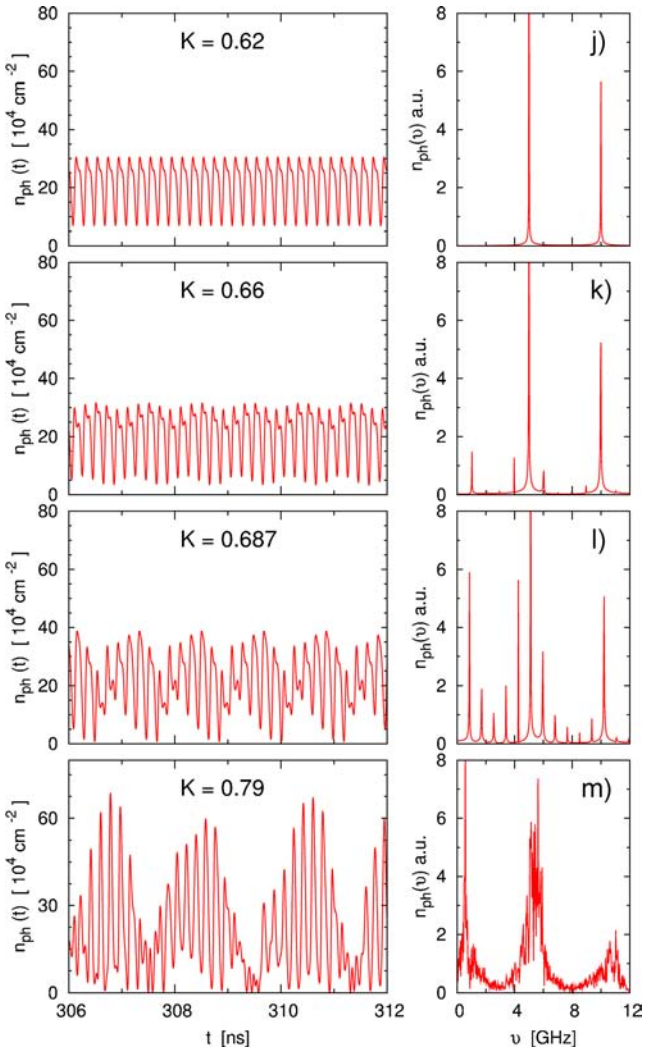

Figure 11 (online color at: www.pss-b.com) Time series (left) and power spectra (right) for selected feedback strengths K: rows (j–m) correspond to $K = 0.62 - 0.79$ as indicated by vertical blue dash-dotted lines (j–m) in the third bifurcation cascade for large $\alpha = 3.2$ and $\Gamma = 0.00225$ in Fig. 3vi.

pulse packages for large α are completely different from the regular pulse packages found in Section 4.1 for small α, which resulted from a homoclinic bifurcation. Thus we do not find a scaling law for the interpulse interval close to the bifurcation point. Instead the frequency of the envelope of the pulse packages $\nu_{PP}(0.79) = 0.58\,\mathrm{GHz}$ is close to the difference of the frequency corresponding to the external cavity roundtrip time and the RO frequency $\nu_{ec} - \nu_{RO}(0.79) = (6.25 - 5.6)\,\mathrm{GHz} = 0.65\,\mathrm{GHz}$, demonstrating that the pulse packages develop out of a torus. Mørk et al. [21] observed experimentally a similar scenario for a QW laser, which they studied also theoretically within a Lang–Kobayashi model. Throughout the third bifurcation cascade the attractor develops "around" the steady state densities of the fourth ECM measured before its Hopf bifurcation point (black dots in Fig. 12). Only after the breakdown of the attractor the system jumps to the stable fifth ECM. Its steady state densities at $K = 0.79$ are indicated by brown circles in the (n_{ph}, $n_{e,h}$)-planes. The steady state WL carrier densities $w_e = 2.15N^{sum}$ and $w_h = 2.45N^{sum}$ are outside the plot range. At $K = 0.7905$ a boundary crisis takes place. This is a global bifurcation in which the chaotic attractor collides with its basin boundary. Directly after the bifurcation we find long chaotic transients (transient chaos) before the system settles down to stable cw operation at the fifth ECM. This is typical for this kind of bifurcation [43]. The fourth bifurcation cascade displays also a quasiperiodic route to chaos similar to the third cascade. Generally, for larger α-factor the ranges of bistability are larger.

5 Dependence of first laser instability on α- and Γ-factor In this section we will focus on the first laser instability and its dependence on the α-factor as well as on the confinement factor Γ. This critical quantity is important because it allows one to quantify the feedback sensitivity of the laser. In Fig. 13a we plot the value of the first Hopf instability (K_c in the bifurcation diagrams of Fig. 3) as a density plot in dependence on the confinement factor Γ and the linewidth enhancement factor α. The value of K_c is color coded: darker color corresponds to higher values of K_c. Thus, the black regions indicate the most stable operation. At first we discuss the dependence on α: using asymptotic methods Levine et al. [41] derived an analytic expression for the lowest bound of the critical feedback strength K_c at which the first ECM loses stability via a Hopf bifurcation:

$$K_c \sim \frac{2\lambda_R}{\sqrt{1+\alpha^2}}. \tag{15}$$

Here, λ_R is the damping rate of the ROs, which will be considered later in this section. Equation (15) basically states that the critical feedback strength decreases with the number of ECMs, since the number of ECMs increases with α. This functional dependence of K_c on α is reproduced in our numeric simulations as can be seen in Fig. 13b that shows the decrease of K_c with α. The solid red line is a fit according to Eq. (15). We also found that changes in the internal QD configuration (different scattering rates and hence different damping rates) have an influence on the bifurcation diagram. Simulations for a QD laser with lower damping rate showed a decreased critical feedback strength K_c as well as small changes in the bifurcation diagram.

The discussion of the confinement parameter Γ is more involved. Figure 13c depicts the dependence of K_c on Γ for two different α-factors. Note that in order to change Γ we varied the geometric confinement factor Γ_g which is accessible in experiments by changing the number of QD layers. As can be seen in this picture the value of K_c first decreases with Γ before it increases for $\Gamma > 0.0038$. Thus, we have two competing processes that have an influence on the critical feedback strength. First, a variation of Γ is accompanied by a change of the WL carrier densities w_e

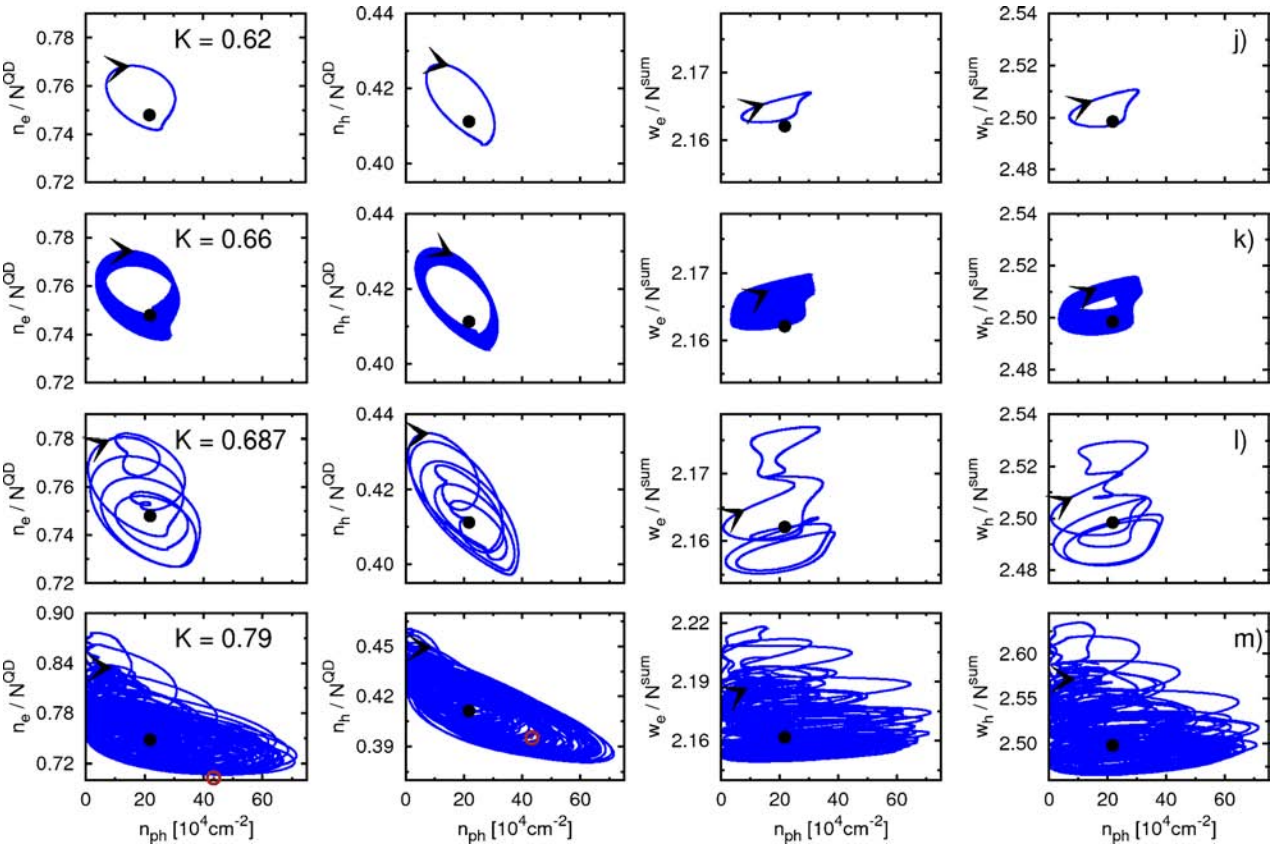

Figure 12 (online color at: www.pss-b.com) Phase space projections of the trajectory onto planes spanned by the photon density n_{ph} and the carrier densities n_e, n_h, w_e, and w_h (column 1–4). Rows (j–m) correspond to $K = 0.62 - 0.79$ as indicated by the vertical dash-dotted lines (j–m) in the third bifurcation cascade for large $\alpha = 3.2$ and $\Gamma = 0.00225$ in Fig. 3vi. Black dots indicate the steady state of the fourth ECM before the supercritical Hopf bifurcation at $K_c = 0.512$. Brown circles indicate the sixth stable ECM at $K = 0.79$.

and w_h at steady state. The higher Γ, the lower are the WL carrier densities which then give rise to larger scattering times τ_e and τ_h (see Ref. [19] for a detailed discussion). Following the asymptotic expansion of Levine et al. [41] the critical feedback is proportional to the damping rate $\lambda_R = 1/2\left(\tau_c^{-1} + \xi P_0\right)$ where P_0 is the photon number, τ_c is the carrier lifetime (here given by τ_e and τ_h) and ξ is the differential gain (in our model given by $\xi = \Gamma WA$). Thus the increase of the scattering times with Γ nicely explains why at first K_c decreases with Γ. Note that this effect cannot be found with a conventional Lang–Kobayashi model with constant carrier lifetime.

However, with further increase of Γ the damping rate is dominated by the second term ξP_0, which is linearly dependent on Γ and is therefore responsible for the increase of K_c that is observed for higher Γ.

6 Comparison of QD and QW lasers In this section we compare the stability properties of a QD laser to those of a QW laser. To model the QW laser we use a conventional Lang–Kobayashi type model with three dynamical variables, namely the photon density n_{ph}, the phase ϕ, and the carrier density n:

$$\dot{n}_{ph} = -2\kappa n_{ph} + \Gamma g_0 (n - n_0) n_{ph} + \beta R_{sp}^{QW}(n) + 2\frac{K}{\tau_{in}}\sqrt{n_{ph,\tau_{ec}} n_{ph}}\cos(\phi - \phi_{\tau_{ec}} + \Theta) \tag{16a}$$

$$\dot{\phi} = \frac{\alpha}{2}\{\Gamma g_0 (n - n_0) - 2\kappa\} - \frac{K}{\tau_{in}}\sqrt{\frac{n_{ph,\tau_{ec}}}{n_{ph}}}\sin(\phi - \phi_{\tau_{ec}} + \Theta) \tag{16b}$$

$$\dot{n} = \frac{j(t)}{e_0} - \frac{1}{\tau_c} n - g_0 (n - n_0) n_{ph}. \tag{16c}$$

For this QW laser model we assume electrons and holes to have the same dynamics. In Eq. (16) n_0 denotes the transparency concentration, which is equal to $N^{QD}/2$ for the QD model, if we set $n = (n_e + n_h)/2$. To compare both lasers the following parameters are used for the QW laser (see Table 1 for numerical values): the linear gain coefficient is set to $g_0 = WA$, the rate of spontaneous emission is modeled by bimolecular recombination $R_{sp}^{QW} = B^S n^2$, and

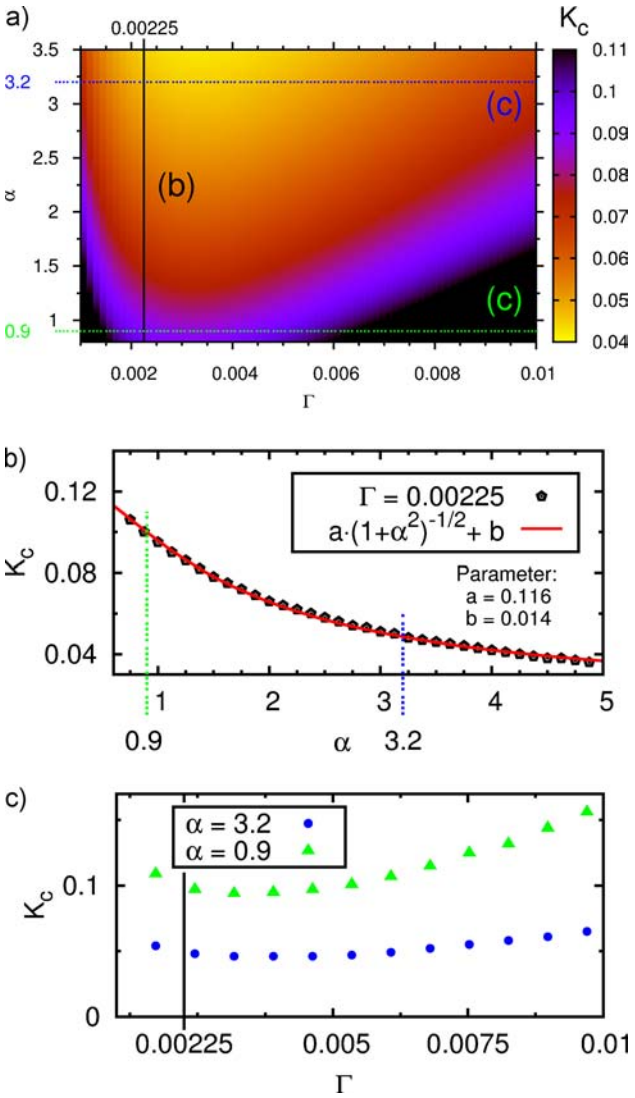

Figure 13 (online color at: www.pss-b.com) (a) Density plot of the critical feedback strength K_c (color coded) at which the first supercritical Hopf bifurcation occurs in dependence of the α- and the Γ-factor. (b) Sections for $\Gamma = 0.00225$ fixed and α varying from 0.6 to 5. (c) Sections for $\alpha = 0.9$ or 3.2 fixed and Γ varying from 0.001 to 0.01.

carrier and photon lifetimes $\tau_c = W^{-1}$ and $\tau_{ph} = (2\kappa)^{-1}$, respectively, are used. Furthermore, the same α-factors and confinement factors Γ as for QD lasers are used in order to enable a direct comparison. (Note, however, that in the case of small $\alpha = 0.9$ this is not necessarily a realistic choice. Also the confinement factor for a realistic QW laser should be larger than for a QD laser.) To determine the steady state photon density of the QW laser n_{ph}^* in dependence of the current density we disregard feedback ($K = 0$) and insert the ECM ansatz ($n_{ph} = n_{ph}^*$, $\phi = \Delta\omega_s t$, and $n = n^*$) in the Eq. (16a–c). By neglecting the spontaneous emission ($\beta = 0$) the photon density is approximately 0 below threshold. Thus Eq. (16c) yields the following expression for the threshold current density:

$$j_{th}^{QW} = \frac{e_0}{\tau_c} n_{th}. \tag{17}$$

Here n_{th} is the carrier density at the laser threshold. Above threshold ($n_{ph}^* \neq 0$) it follows from Eq. (16a) that the carrier density is clamped to its threshold value:

$$n^* = n_{th} = n_0 + \frac{2\kappa}{\Gamma g_0}.$$

Following Eq. (16c), the steady state characteristic for the photon density can be determined by:

$$n_{ph}^* = \Gamma\tau_{ph}(J-1)\frac{j_{th}^{QW}}{e_0}, \tag{18}$$

where $J = j/j_{th}^{QW}$ is the injection current density normalized to its threshold value. For comparison of the QW and QD laser models we calculate j_{th}^{QW} and n_{th} from Eqs. (18) and (17), respectively, by setting the steady state value n_{ph}^* of the photon density equal for both lasers.

Figure 14 shows the response of the QW (red dashed line) and the QD laser (solid blue line) to a current pulse (brown dash-dotted line) of 6 ns width. Both lasers are pumped at a current density of 2.5 j_{th}. It can be seen that for this parameter set the QW laser displays less damping and a higher RO frequency than the QD laser, as expected from experiments. The response of the QW laser to optical feedback for given α is qualitatively similar to the response of the QD laser. The bifurcation diagrams of the QW laser display the same number of bifurcation cascades, starting from Hopf points and evolving into chaos, as in the case of the QD laser. This was expected, because both laser systems have the same basic solutions (ECMs). Thus in the following we concentrate on the first bifurcation cascades. In Fig. 15 the first instability regimes of n_{ph} in dependence of the feedback strength K are depicted for both lasers. Figure 15a and b show the instabilities for small $\alpha = 0.9$ and Fig. 15c and d for large $\alpha = 3.2$. The middle panels of Fig. 15 depict the

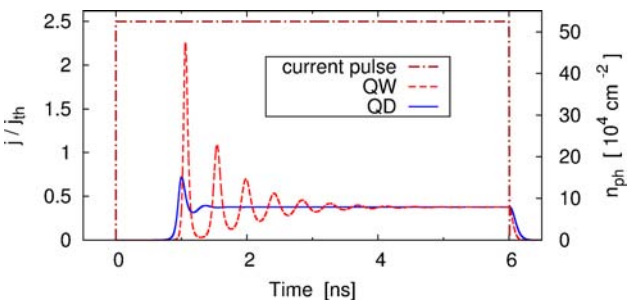

Figure 14 (online color at: www.pss-b.com) Response of photon density to a rectangular current density $j(t)$ pulse of 6 ns width and $j/j_{th} = 2.5$ (brown dash-dotted line) for a QD laser (solid blue line) and a QW laser (red dashed line). $j(t)$ is normalized to the threshold current density of the laser. For both cases the parameters of Table 1 are used. Additionally the steady state photon density of the QW laser has been set to the value of the QD laser ($K = 0$).

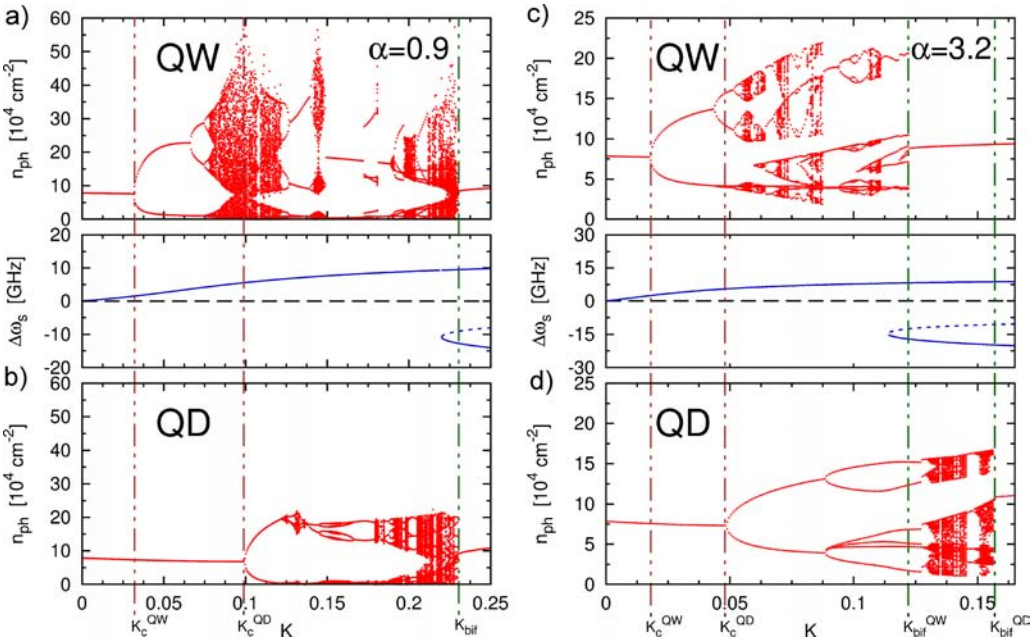

Figure 15 (online color at: www.pss-b.com) First bifurcation cascades of the photon density n_{ph} (red) for a QW laser (upper panels) and a QD laser (lower panels) in dependence of the feedback strength K for small $\alpha = 0.9$ (a and b) and large $\alpha = 3.2$ (c and d). Middle panels: frequency deviations $\Delta\omega_s$ of the possible external cavity modes (blue). Brown vertical dash-dotted lines mark the Hopf bifurcation. Green vertical dash-dotted lines mark the ends of the bifurcation cascades.

frequency deviations $\Delta\omega_s$ of the possible ECMs. In Fig. 15a and c it can be seen that the QW laser takes a period-doubling route to chaos like the QD laser (Fig. 15b and d). Nevertheless the critical feedback strengths, at which the supercritical Hopf bifurcation occurs, are lower for the QW laser than for the QD laser (brown vertical dash-dotted lines in Fig. 15). For small $\alpha = 0.9$ the critical feedback strength for the QW laser is $K_c^{QW} = 0.032$ (but $K_c = 0.099$ for the QD laser) and for large $\alpha = 3.2$ it is $K_c^{QW} = 0.018$ (but $K_c = 0.048$ for the QD laser). For small α the QW laser is already in the chaotic regime while the QD laser becomes unstable. In the chaotic regime the photon density of the QW laser performs stronger oscillations due to the weaker damping of the ROs.

For small α the second ECM mode becomes stable in a homoclinic bifurcation for both lasers at the same value of the feedback strength $K_{bif} = 0.2305$ (green vertical dash-dotted lines in Fig. 15i and ii). Thus for feedback strengths slightly lower than $K_{bif} = 0.2305$ both lasers display strictly regular pulse packages as described in Section 4.1.2.

For large $\alpha = 3.2$ the QW laser is stabilized again by a homoclinic bifurcation, in which the system settles down to the newly born second ECM at $K_{bif}^{QW} = 0.128$. In this case the strictly regular pulse packages develop out of a periodic window at $K = 0.117$ when the second mode-antimode pair is created. In contrast, the QD laser stays chaotic until it settles down to the second mode at $K_{bif}^{QD} = 0.157$ in a boundary crisis. If we choose the carrier lifetime such that the QW laser has the same damping, both lasers have nearly identical critical feedback strengths. This demonstrates that for equal parameters including the α-factor the QD laser is more tolerant to feedback due to its strongly suppressed ROs, which is in accordance with Ref. [6].

7 Conclusion Combining a Lang–Kobayashi like field equation with microscopically based carrier rate equations, we can explain the reduced feedback sensitivity found in QD devices on the one hand by its strongly damped ROs and on the other hand by the relatively small number of ECMs for a given external cavity round trip time τ_{ec}. The small number of ECMs originates from a weaker phase–amplitude coupling compared to QW devices. For QD lasers with large linewidth enhancement factor $\alpha > 3$ we find a bifurcation cascade leading to chaotic regions alternating with short regions of stable cw operation. This resembles the behavior typical for QW devices [23]. For low $\alpha \approx 1$ the model exhibits reduced feedback sensitivity and performs stable cw operation over a wide range of increasing feedback strength. Moreover, for low α we found intensity pulsations in a certain range of the feedback strength which are strictly regular for $\alpha \leq 0.9$ and become more irregular with increasing α.

Acknowledgements This work was supported by DFG within Sfb 787.

Appendix A
Fit functions for the microscopically calculated scattering rates

$$S_e^{in}(w_e, w_h) = -8.4 \times 10^{-4}\,\mathrm{ps}^{-1} + w_e 7.2 \times 10^{-15}\,\mathrm{ps}^{-1}\,\mathrm{cm}^2 + w_h 5.4 \times 10^{-15}\,\mathrm{ps}^{-1}\,\mathrm{cm}^2 \quad (19a)$$

$$S_{\mathrm{h}}^{\mathrm{in}}(w_{\mathrm{e}}, w_{\mathrm{h}}) = w_{\mathrm{h}} 8.9 \times 10^{-15}\,\mathrm{ps}^{-1}\,\mathrm{cm}^2 + w_{\mathrm{h}}^2 2.6 \times 10^{-26}\,\mathrm{ps}^{-1}\,\mathrm{cm}^4 - w_{\mathrm{h}}^3 5.74 \times 10^{-39}\,\mathrm{ps}^{-1}\,\mathrm{cm}^6 \quad (19b)$$

In the fit function Eq. (19b) the dependence on w_{e} was found to be negligible:

$$S_{\mathrm{e}}^{\mathrm{out}}(w_{\mathrm{e}}, w_{\mathrm{h}}) = S_{\mathrm{e}}^{\mathrm{in}}(w_{\mathrm{e}}, w_{\mathrm{h}}) \times \mathrm{e}^{-101\,\mathrm{meV}/26\,\mathrm{meV}} \left[\mathrm{e}^{w_e/(4.7\times 10^{11}\,\mathrm{cm}^{-2})} - 1\right]^{-1} \quad (19c)$$

$$S_{\mathrm{h}}^{\mathrm{out}}(w_{\mathrm{e}}, w_{\mathrm{h}}) = S_{\mathrm{h}}^{\mathrm{in}}(w_{\mathrm{e}}, w_{\mathrm{h}}) \times \mathrm{e}^{-54\,\mathrm{meV}/26\,\mathrm{meV}} \left[\mathrm{e}^{w_{\mathrm{h}}/(48\times 10^{11}\,\mathrm{cm}^{-2})} - 1\right]^{-1} \quad (19d)$$

References

[1] D. Bimberg, M. Grundmann, and N. N. Ledentsov, Quantum Dot Heterostructures (John Wiley & Sons Ltd., New York, 1999).
[2] W. W. Chow and S. W. Koch, Semiconductor-Laser Fundamentals (Springer, Berlin, 2004).
[3] M. R. Dachner, E. Malić, M. Richter, A. Carmele, J. Kabuß, A. Wilms, J. E. Kim, G. Hartmann, J. Wolters, U. Bandelow, and A. Knorr, Phys. Status Solidi B **247**, No. 4 (2010), this issue.
[4] D. O'Brien, S. P. Hegarty, G. Huyet, J. G. McInerney, T. Kettler, M. Lämmlin, D. Bimberg, V. Ustinov, A. E. Zhukov, S. S. Mikhrin, and A. R. Kovsh, Electron. Lett. **39**, 25 (2003).
[5] D. O'Brien, S. P. Hegarty, G. Huyet, and A. V. Uskov, Opt. Lett. **29**(10), 1072–1074 (2004).
[6] G. Huyet, D. O'Brien, S. P. Hegarty, J. G. McInerney, A. V. Uskov, D. Bimberg, C. Ribbat, V. M. Ustinov, A. E. Zhukov, S. S. Mikhrin, A. R. Kovsh, J. K. White, K. Hinzer, and A. J. SpringThorpe, Phys. Status Solidi B **201**(2), 345–352 (2004).
[7] O. Carroll, I. O'Driscoll, S. P. Hegarty, G. Huyet, J. Houlihan, E. A. Viktorov, and P. Mandel, Opt. Express **14**(22), 10831–10837 (2006).
[8] M. Radziunas, A. Glitzky, U. Bandelow, M. Wolfrum, U. Troppenz, J. Kreissl, and W. Rehbein, IEEE J. Sel. Top. Quantum Electron. **13**(1), 136–142 (2007).
[9] O. Ushakov, S. Bauer, O. Brox, H. J. Wünsche, and F. Henneberger, Phys. Rev. Lett. **92**, 043902 (2004).
[10] D. M. Kane, K. A. Shore (eds.), Unlocking Dynamical Diversity: Optical Feedback Effects on Semiconductor Lasers (Wiley-VCH, Weinheim, 2005).
[11] G. H. M. van Tartwijk, and G. P. Agrawal, Prog. Quantum Electron. **22**(2), 43–122 (1998).
[12] S. Wieczorek, B. Krauskopf, T. Simpson, and D. Lenstra, Phys. Rep. **416**(1–2), 1–128 (2005).
[13] S. Schikora, P. Hövel, H. J. Wünsche, E. Schöll, and F. Henneberger, Phys. Rev. Lett. **97**, 213902 (2006).
[14] V. Flunkert and E. Schöll, Phys. Rev. E **76**, 066202 (2007).
[15] T. Dahms, P. Hövel, and E. Schöll, Phys. Rev. E **76**(5), 056201 (2007).
[16] T. Dahms, P. Hövel, and E. Schöll, Phys. Rev. E **78**(5), 056213 (2008).
[17] B. Fiedler, S. Yanchuk, V. Flunkert, P. Hövel, H. J. Wünsche, and E. Schöll, Phys. Rev. E **77**(6), 066207 (2008).
[18] V. Flunkert, O. D'Huys, J. Danckaert, I. Fischer, and E. Schöll, Phys. Rev. E **79**, 065201 (R) (2009).
[19] K. Lüdge and E. Schöll, IEEE J. Quantum Electron. **45**(11), 1396–1403 (2009).
[20] R. Lang and K. Kobayashi, IEEE J. Quantum Electron. **16**, 347 (1980).
[21] J. Mørk, B. Tromborg, and J. Mark, IEEE J. Quantum Electron. **28**, 93 (1992).
[22] T. Sano, Phys. Rev. A **50**(3), 2719–2726 (1994).
[23] A. Hohl and A. Gavrielides, Phys. Rev. Lett. **82**, 1148–1151 (1999).
[24] D. Pieroux, T. Erneux, B. Haegeman, K. Engelborghs, and D. Roose, Phys. Rev. Lett. **87**, 19, (2001).
[25] T. Heil, I. Fischer, W. Elsäßer, B. Krauskopf, K. Green, and A. Gavrielides, Phys. Rev. E **67**, 066214 (2003).
[26] E. A. Viktorov, P. Mandel, and G. Huyet, Opt. Lett. **32**(10), 1268–1270 (2007).
[27] N. Schunk and K. Petermann, IEEE Photonics Technol. Lett. **1**(3), 49–51 (1989).
[28] R. J. Jones, P. S. Spencer, J. Lawrence, and D. M. Kane, IEE Proc. Optoelectron. **148**(1), 7–12 (2001).
[29] G. H. M. van Tartwijk, A. M. Levine, and D. Lenstra, IEEE J. Sel. Topics Quantum Electron. **1**(2), 466 (1995).
[30] T. Heil, I. Fischer, W. Elsäßer, and A. Gavrielides, Phys. Rev. Lett. **87**, 243901 (2001).
[31] E. Malić, M. J. P. Bormann, P. Hövel, M. Kuntz, D. Bimberg, A. Knorr, and E. Schöll, IEEE J. Sel. Top. Quantum Electron. **13**(5), 1242–1248 (2007).
[32] K. Lüdge, M. J. P. Bormann, E. Malić, P. Hövel, M. Kuntz, D. Bimberg, A. Knorr, and E. Schöll, Phys. Rev. B **78**(3), 035316 (2008).
[33] G. H. M. van Tartwijk, and D. Lenstra, Quantum Semiclass. Opt. **7**, 84 (1995).
[34] C. W. Gardiner, Handbook of Stochastic Methods (Springer, Berlin, Heidelberg, New York, 1985).
[35] B. Krauskopf and D. Lenstra (eds.), Fundamental Issues of Nonlinear Laser Dynamics, AIP Conference Proceedings 548 (American Institute of Physics, Melville, New York, 2000).
[36] B. Krauskopf, G. H. M. van Tartwijk, and G. R. Gray, Opt. Commun. **177**(1–6), 347 (2000).
[37] G. Lythe, T. Erneux, A. Gavrielides, and V. Kovanis, Phys. Rev. A **55**(6), 4443–4448 (1997).
[38] V. Rottschäfer and B. Krauskopf, Int. J. Bif. Chaos **17**(5), 1575–1588 (2007).
[39] Y. A. Kuznetsov, Elements of Applied Bifurcation Theory (Springer, New York, 1995).
[40] J. Hizanidis, R. Aust, and E. Schöll, Int. J. Bifur. Chaos **18**(6), 1759–1765 (2008).
[41] A. M. Levine, G. H. M. van Tartwijk, D. Lenstra, and T. Erneux, Phys. Rev. A **52**(5), R3436–R3439 (1995).
[42] D. Pieroux, T. Erneux, A. Gavrielides, and V. Kovanis, SIAM J. Appl. Math. **61**(3), 966–982 (2000).
[43] C. Grebogi, E. Ott, and J. A. Yorke, Physica D **7**, 181–200 (1983).